

FINAL YEAR PROJECT REPORT

NAME:	Alex Higginbottom
DEGREE COURSE:	Physics (Msci)
PROJECT TITLE:	Cooling to Zero
YEAR OF SUBMISSION:	2023
SUPERVISOR:	Antony Carrington
NUMBER OF WORDS:	9218



Declaration

We did not machine the ADR ourselves. Parts were machined by Jake Rusby from the mechanical workshop. Also, the FAA pill with which we collected all our final data was not assembled by us, but was passed on from the previous group who completed this Msci project.

We received practical assistance in leak checking, magnet cooling and general cryogenics from Joe Wilcox, Tobias Chatfield (PhD student) and our supervisor, Prof. Tony Carrington, who also wrote a Delphi code for us to operate the magnet, so we could collect data overnight in the final weeks.

Acknowledgements

I would like to thank Jake Rusby from the mechanical workshop for aiding us with practical concerns of our design, as well as manufacturing the parts. I would also like to thank Tom Kennedy for his constant desire to help us achieve the best we can, and doing as much as he can to facilitate that. I would also like to thank Joe Wilcox and Tobias Chatfield for their unending patience for myself and my lab partner, and helping us with myriad practical issues. Finally, I would like to thank our supervisor, Prof. Antony Carrington, for his guidance and good humour.

Abstract

This project aimed to design, optimise and construct an inexpensive adiabatic demagnetisation refrigerator (ADR), capable of reaching temperatures below what is achievable with liquid helium. As part of this goal, a gas-gap heat switch was constructed and tested, achieving an on : off thermal conductance ratio of 27.3. However, due to an excessive heat leak from getter operation, this could not be implemented for ADR. Changes required for successful implementation are discussed.

The minimum temperature reached during demagnetisation was 0.43 ± 0.03 K, using a superconducting lead heat switch. With superconducting niobium, a greater temperature change was achieved, cooling from 2.040 ± 0.007 K to 0.49 ± 0.03 K – demonstrating the potential of niobium as a heat switch. A comparison is made between lead and niobium superconducting heat switches, and the main inefficiencies are identified for each using a thermal model. Finally, recommended design changes are identified to improve the performance of the ADR.

Contents

1	Introduction	1
1.1	Magnetic cooling	1
1.1.1	ADR cycle	2
2	Paramagnetism and salt choice	3
2.1	The free-ion approximation	3
2.1.1	The Thermodynamics of Adiabatic Demagnetisation	3
2.1.2	The Thermodynamics of Isothermal Magnetisation	4
2.2	Pill Construction	4
2.2.1	Salt choice	4
2.2.2	Thermal bus	6
2.2.3	Crystal growth	7
2.2.4	Pill housing	8
2.2.5	Future work	8
3	Gas-gap heat switch	9
3.1	Background	9
3.1.1	Thermal conductivity	9
3.1.2	Adsorption pump	10
3.1.3	Gas choice	10
3.1.4	Design	10
3.1.5	Experimental methods	13
3.1.6	Results	14
3.1.7	Discussion	17
3.2	Conclusions	17
4	Refrigeration	18
4.1	Design	18
4.1.1	Lead heat switch	18
4.1.2	Niobium heat switch	19
4.1.3	Design model	20
4.2	Experimental methods	22
4.3	Results	23
4.3.1	Lead heat switch	23
4.3.2	Niobium heat switch	25
4.3.3	Errors	25
4.4	Discussion	26
4.4.1	ADR performance	26
4.4.2	Lead switch performance	27
4.4.3	Niobium switch performance	29
4.5	Modelling	29
4.5.1	Construction of the model	30
4.5.2	Pill Characterisation	31
4.5.3	Field-dependence	32
4.5.4	Heat leak contributions	33
4.6	Improvements	34
4.7	Conclusions	35
5	Appendix	36
A	Errors	36
A.1	Magnetoresistance of ROX chip resistors	36
A.2	GGHS thermometer error	36
A.3	Systematic error on ROX	36
B	Internal field approximation	37
C	Full demagnetisation results	37

1 Introduction

Since the liquefaction of Helium by Kamerlingh-Onnes in 1908 [1], the development of new techniques for accessing ever lower temperatures has paved the way for the realisation of countless groundbreaking phenomena, notably superconductivity, the Josephson effect, and the experimental observation of Bose-Einstein condensation as recently as 1995. One such leap was the theoretical underpinning of adiabatic demagnetisation refrigeration (ADR) by Debye in 1926 and Giauque in 1927 [2]. Since then, ADR has seen employment in a vast array of applications, including high-sensitivity space telescopes and quantum computers [3], and now exists as one of the most common methods for accessing very low temperatures.

The other primary technique is dilution refrigeration. This technology emerged in the 1960s and has become the de-facto method for cooling to the <1 K range, especially for continuous operation [4]. Dilution refrigeration operates using a mixture of two helium isotopes, helium-3 (^3He) and helium-4 (^4He). The refrigeration process involves diluting ^4He atoms into a concentrated phase of ^4He at low temperatures, absorbing heat from the surroundings in an endothermic reaction [5]. The ^4He is then extracted from the mixture, allowing for continuous, stable ultra-low temperature cooling. In recent years, however, the price of ^3He has increased significantly [6], leading to higher operational costs for dilution refrigeration.

As a result, there is an economic incentive for developing an alternative, that can operate in the same temperature range, particularly for lab use. ADR, despite being a mature technology, has seen little development with cost and practicality as leading design requirements. This project aims to produce an ADR using readily available, low-cost materials whilst reliably cooling to below what is achievable by simply reducing the vapour pressure of helium ($\sim 0.3\text{K}$) [5].

To this end, this report has four main sections. Section one outlines the background and key theoretical ideas. Section two focuses on the theory of paramagnetism, and the design and construction of a paramagnetic salt pill. Section three presents the design, construction, and testing of a gas-gap heat switch (GGHS). Finally, section four presents the key experimental refrigeration results, and outlines a modelling approach to determine the main sources of inefficiency for future improvement.

1.1 Magnetic cooling

Any cooling system can be thought of as a way to reduce a system's entropy. In the case of ADR, this is achieved by aligning the magnetic moments of a naturally disordered system. By definition, it is thus the paramagnetic material, and its field dependence, that drives the refrigeration. Consequently, careful selection and implementation of the paramagnetic material is key.

Typically, there is a large paramagnetic response for atoms or ions lacking, or possessing an odd number of, electrons. These magnetic ions interact weakly, such that their interaction energy is less than the average energy of random thermal fluctuations in the lattice, $k_B T$ (where k_B is Boltzmann's constant). Thus, the ions in a paramagnetic material are essentially free, and can occupy any one of the $2J+1$ spatial orientations available, where J is the total angular momentum quantum number, and their entropy can be described by

$$S_m = R \ln(2J + 1), \quad (1)$$

where R is the gas constant. In general, the total entropy is the sum of magnetic, S_m , lattice, S_{lattice} , and electric S_e , components,

$$S = S_m + S_{\text{lattice}} + S_e. \quad (2)$$

At temperatures of a few kelvins, the magnetic term dominates, so $S_{\text{tot}} \approx S_m$, and the entropy per mole simply given by eq. (1). However, as $T \rightarrow 0$, there is a point where the thermal energy, $k_B T$, will become significant, and it becomes favourable for the dipoles to spontaneously order and lower the total entropy. This critical point is called the Curie or Neel temperature (for a ferromagnetic or antiferromagnetic transition, respectively), at which point no further cooling can be achieved by demagnetisation [7].

The degree of ordering is inversely related to the strength of forces between adjacent ions. In this region, interaction energies are significant, meaning that an applied field of only a few Tesla can considerably enhance ordering. Thus, the entropy change upon isothermal magnetisation is substantial, leading to a significant temperature change during adiabatic demagnetization (see fig. 1). This maximum in the entropy change also increases the heat capacity for a given applied field, B , and temperature, T ,

$$C_B = T \left(\frac{\partial S}{\partial T} \right)_B, \quad (3)$$

which can also be beneficial as it reduces the effect of heat leaks on the system, particularly for maximising the low temperature hold-time. It is important to note that the magnitude of the interaction energies is dependent on the material and temperature in question. For the purposes of this project, effective refrigeration is desired for the range $0.1 \text{ K} < T < 1.5 \text{ K}$. By considering the magnetic form of the first law of thermodynamics, the change in entropy with an applied field in such a system can be described by the Langevin expression,

$$\left(\frac{\partial T}{\partial B}\right)_S = -\frac{T}{C} \left(\frac{\partial M}{\partial T}\right)_B, \quad (4)$$

where M is the magnetisation.

1.1.1 ADR cycle

By exploiting the relation given in eq. (4), a paramagnetic material can be used for refrigeration via the ADR cycle. A theoretical ideal cycle is given below.

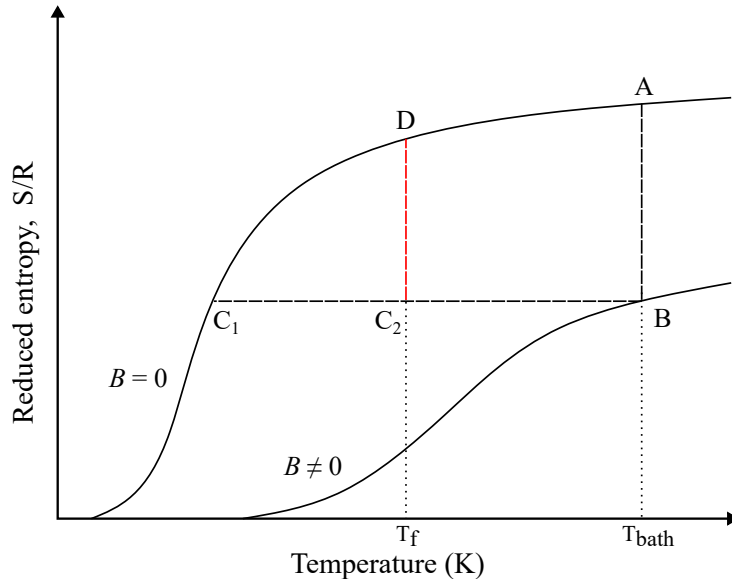


Figure 1: Sketch of an idealised entropy vs temperature diagram for a typical paramagnetic material.

I) At the starting point, A, the salt pill is in thermal equilibrium ($\sim 1.5\text{K}$) with the heat sink in zero magnetic field ($B = 0$).

II) A \rightarrow B. With the system in thermal equilibrium, the magnetic field is isothermally ramped up to a maximum value, B_i . The heat induced by magnetisation is dissipated into a heat bath. The ions align with the field and magnetic entropy decreases to a minimum.

III) B \rightarrow C₁ or C₂. The magnetic field is adiabatically decreased. The lattice temperature of the salt falls to the desired final temperature, T_f , (C₁ for ‘single-shot’ or C₂ for holding at T_f) as entropy is transferred from the lattice to the magnetic moments.

IV) C₂ \rightarrow D. To hold at T_f . The remaining magnetic field can be decreased to balance any heat leaks to maintain constant temperature. Once $B = 0$, the hold time has finished.

V) C₁ or D \rightarrow A. With $B = 0$, the system warms back to T_i [8].

2 Paramagnetism and salt choice

To optimise the refrigeration achieved by this cycle, the paramagnetic material must be carefully selected and implemented. This section will outline the theory of the thermodynamics of paramagnetic materials at low temperature, the design motivation, and describe the experimental method of the pill construction.

2.1 The free-ion approximation

Although eq. (4) provides a description of the physics of demagnetisation refrigeration, it is useful to express it in easily measurable quantities, such as the applied magnetic field. This is achieved by considering the partition function for independent magnetic dipoles (see ??), resulting in an expression that describes a system for general J , the ‘free-ion approximation’,

$$\frac{S(B, T)}{R} = x \coth x - (2J + 1)x \coth(2J + 1)x + \ln \frac{\sinh(2J + 1)x}{\sinh x}, \quad (5)$$

where

$$x = \frac{g\mu_B B}{2k_B T}. \quad (6)$$

Here μ_B is the Bohr magneton and g the Landé factor. For small fields, (i.e. applying small angle approximations), eq. (1) is returned as expected.

2.1.1 The Thermodynamics of Adiabatic Demagnetisation

The probability that a dipole will occupy one of the $2J + 1$ orientations is given by the Boltzmann factor,

$$\exp\left(-\frac{\epsilon}{k_B T}\right), \quad (7)$$

where ϵ is taken to be $\epsilon = \mu_B g B$. As the process is theoretically adiabatic, the Boltzmann factors must be equal before and after demagnetisation,

$$\exp\left(-\frac{m\mu_B g B_i}{k_B T_i}\right) = \exp\left(-\frac{m\mu_B g B_f}{k_B T_f}\right), \quad (8)$$

where T_i , T_f , and B_i , B_f correspond to the initial and final demagnetisation temperatures and fields, respectively. The final temperature, can then be given by

$$T_f = T_i \frac{B_f}{B_i}. \quad (9)$$

This formulation breaks down as $T \rightarrow 0$ as the assumption of negligible interactions between ions is no longer valid. To rectify this, the internal field b generated by the interactions within the paramagnetic salt must be considered. We can replace the final field with an effective field [9],

$$T_f = \frac{T_i}{B_i} \sqrt{B_f^2 + b^2}, \quad (10)$$

where b is a material-dependent and can be approximated by

$$b = \frac{k_B T_c}{\mu_B}, \quad (11)$$

and is typically ~ 10 s of mT [10]. This result is derived from the Curie law, so it breaks down at high fields. The magnitude of this value will vary for different materials depending on the nature of the interactions and spacing of ions, but should be minimised to achieve a lower T_f . Salts are aqueous, meaning their ion spacing is relatively large and can be tuned, making them apt for use in ADRs.

Once the applied field is zero, the salt will gradually begin to warm up. The heat absorbs as it warms is equivalent to the cooling power of the salt, given by

$$Q(B_f) = n \int_{T_f}^{T_b} T \left(\frac{\partial S}{\partial T} \right)_{B_f} dT, \quad (12)$$

where T_b is the temperature of the thermal bath, and n is the number of moles of the paramagnetic material.

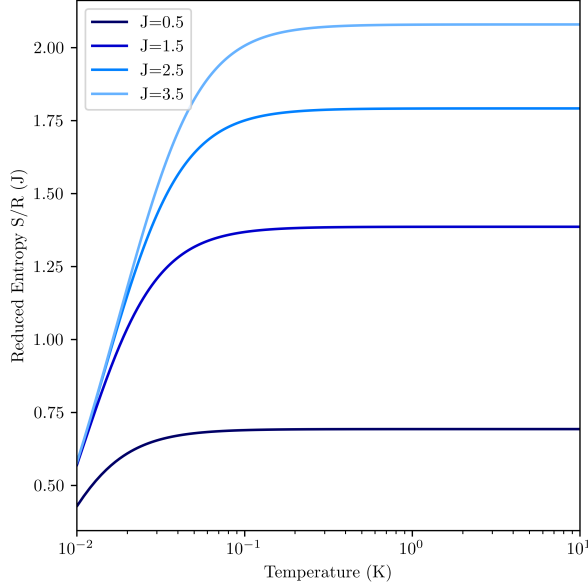


Figure 2: Effect of different J values on the entropy according to the free-ion approximation with $B = b$.

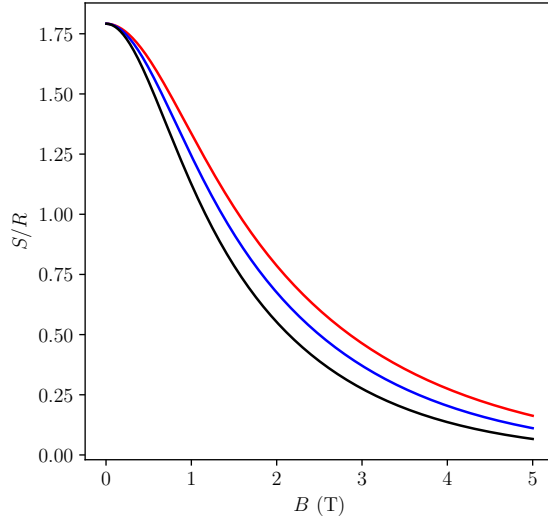


Figure 3: Free-ion entropy vs field for FAA at various temperatures. These temperatures are initial temperatures T_i for different demagnetisations (see section 4.3).

2.1.2 The Thermodynamics of Isothermal Magnetisation

The heat generated by magnetising the salt from zero to B_i is given by

$$Q(T_b) = nT_b \int_0^{B_i} \left(\frac{\partial S}{\partial B} \right)_{T_B} dB, \quad (13)$$

where T_b is the temperature of the thermal bath and n is the number of moles.

2.2 Pill Construction

2.2.1 Salt choice

It is the entropy change of the paramagnetic salt in a given temperature range that drives the cooling of an ADR. Careful selection is, therefore, paramount. The most important properties that need to be considered are as follows;

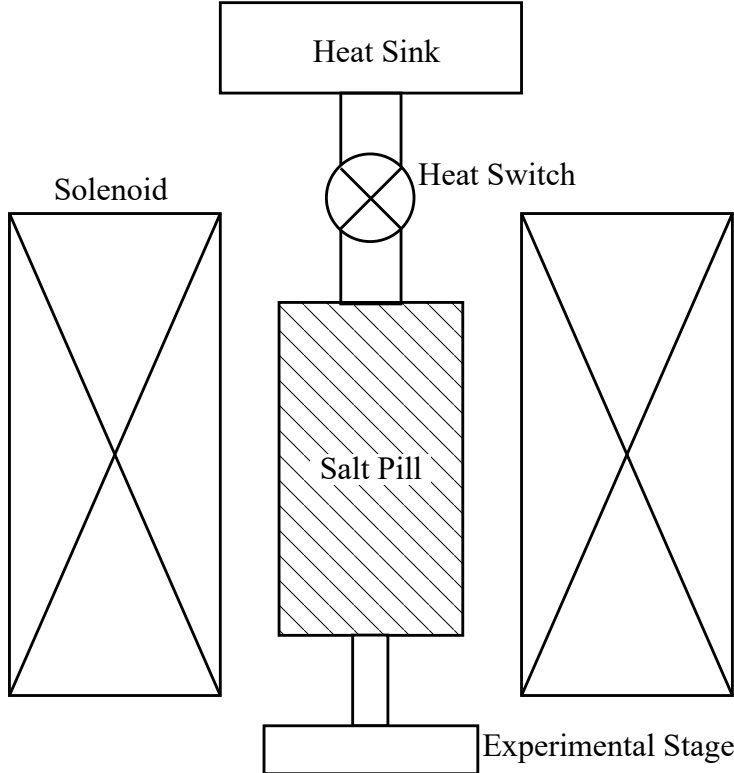


Figure 4: Schematic diagram of a typical single stage ADR. Salt pill and heat switch are within a superconducting solenoid.

- The magnitude of the magnetocaloric effect in the relevant temperature range. This is dependent on two factors:
 - J value. A larger J value increases the entropy of the paramagnetic material at zero-field (see fig. 2) and hence offers greater potential for reduction in entropy upon application of a field.
 - The value of T_N . T_N must be sufficiently close to the temperature range in which the system operates to benefit from a large $\partial M/\partial T$, but must be sufficiently far away to avoid spontaneous entropy reduction. The value of T_N also sets a theoretical limit on the minimum achievable temperature (see eq. (10)).
- High thermal conductivity to minimize temperature gradients.
- Specific heat capacity. A large specific heat capacity is beneficial for minimising the effect of heat leaks, while a smaller specific heat capacity allows for greater $\partial T/\partial B$ (see eq. (4)). A tradeoff must be found depending on the requirements of the ADR.
- Practicality of experimental implementation. Factors such as interactions with other construction materials, ease of crystal growth, packing fraction, and cost must also be considered.

With these factors in mind, there are three main groups available: the Alums, Perovskites, and Garnets. In the Alums, due to the relatively large magnetic moment spacing, the dipole-dipole and exchange interactions are typically weak, meaning their ordering temperature is very low. In comparison, the Garnets and Perovskites have a higher ordering temperature, thus are more suitable for higher temperature ADRs (e.g. 1 – 15 K) and will not be considered further here.

The two most viable and widely used alums in ADRs are FAA and CPA (see table section 2.2.1). Due to their large entropy change and low Neel temperatures, they are ideal for low-temperature ADR operation [11]. FAA in particular has a high $\partial S/\partial T < 2$ K, owing to its larger value for J (see figure fig. 2), but has a higher T_N and maximum specific heat capacity than CPA (see fig. 5). FAA is thus better suited to slightly higher temperatures, and cannot achieve as low T_f , although still well below the 100 mK target of this project.

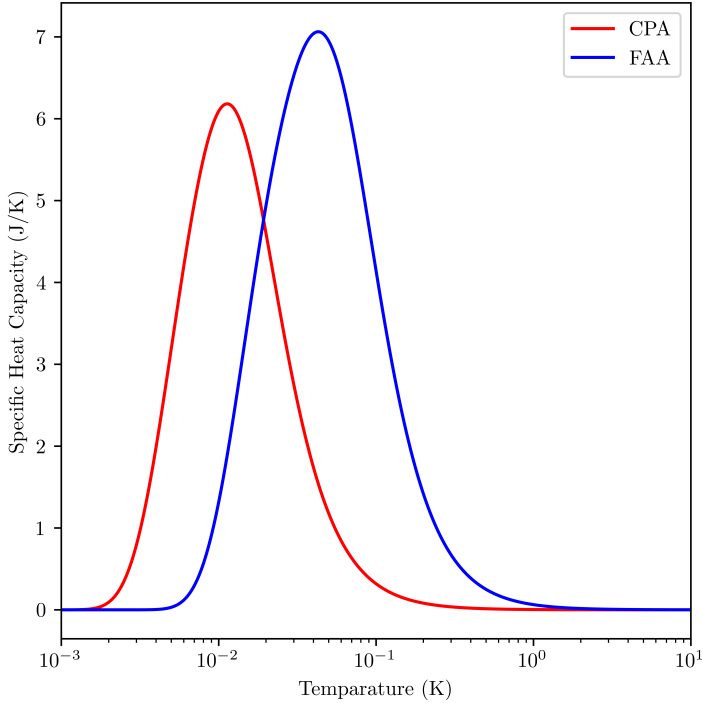


Figure 5: Specific heat capacity of FAA and CPA with zero applied field according to the free-ion approximation with b from eq. (11).

Refrigerant	Chemical Formula	J	g	T_N (mK)	b (mT)	ρ (gcm $^{-3}$)
CMN	Ce ₂ Mg ₃ (NO ₃) ₁₂ 24H ₂ O	1/2	2	1 [8]	4 [12]	2.09
CPA	CrK(SO ₄) ₂ .12H ₂ O	3/2	2	9 [8]	34 [13]	1.83
CCA	CrCs(SO ₄) ₂ 12H ₂ O	3/2	2	10 [8]	2*	2.06
FAA	Fe(NH ₄)(SO ₄) ₂ .6H ₂ O	5/2	2	26 [8]	50 [14]	1.71
MAS	Mn(SO ₄) ₂ (NH ₄) ₂ 6H ₂ O	5/2	2	170 [8]	253*	1.81
DGG	Dy ₃ Ga ₅ O ₁₂	1/2	8	373 [8]	16 [15]	7.308
GGG	Gd ₃ Ga ₅ O ₁₂	7/2	2	800 [8]	1190*	7.14

Table 1: Properties of paramagnetic salts commonly used in ADR. Starred values were calculated using eq. (11) and should only be used as an order of magnitude estimate. Densities, ρ , obtained from [8].

A significant issue with using FAA, however, is that it is corrosive to copper – in one case it was found to fully corrode a 500 μ m gold-plated copper tube in five days [16]. This challenge is exacerbated by the fact that due to its thermal properties, copper and copper-based alloys are extremely useful in ADR construction, and using FAA forces design compromises as a result. CPA, on the other hand, does not corrode copper and exhibits similar properties to FAA [17]. Importantly, of the options presented in section 2.2.1, they are the cheapest and most readily available.

2.2.2 Thermal bus

To harness the cooling generated in the salt and thermally connect it to an experimental stage (ES), a thermal bus must be used. Since any experiments or measurements take place at the ES, the bus design is critical. Poor thermal connection between the salt and stage results in slower thermal response, increasing the effect of heat leaks and reducing the minimum temperature and hold time at the stage. Additionally, high thermal contact within the pill itself is important to ensure an even rate of heat transfer during magnetisation and demagnetisation.

As FAA and CPA are non-electrically conducting, thermal conduction is dominated by phonons. The resulting thermal transfer is given by [18, 19]

$$\frac{dQ}{dt} = \frac{\beta A}{3}(T_1^3 - T_2^3), \quad (14)$$

Component	Material	Diameter (individual, mm)	Length (individual, mm)	κ (W/m/K) (1 K)	Eddy current (W) ($dB/dt = 0.5\text{T}/\text{min}$)
Bus wires	Cu (RRR ≈ 100)	0.25×10^{-7}	66	5 [5]	4.94×10^{-9}
Linking wire	Cu (RRR ≈ 40)	1.1	47	5 [5]	0.586

Table 2: Physical properties and eddy current contributions of thermal bus and experimental stage-pill link.

where $T_1 - T_2$ is the temperature difference across the boundary and β is the thermal transport parameter with a typical value of $\sim 5 \times 10^4 \text{ Wcm}^{-2}\text{K}^{-3}$ [20].

An additional consideration is eddy currents generated by the changing magnetic field must be mitigated, which can be determined for a solid rod geometry using the relation [21],

$$Q_e = \left(\frac{dB}{dt} \right)^2 \frac{\pi r^4 h}{8\rho}, \quad (15)$$

where ρ is the electrical resistivity of the material. According to the Wiedemann–Franz law, the thermal conductivity and are directly proportional for metals [22]. As the thermal conductivity must be maximised, the geometry of the thermal bus must be optimised to minimise eddy currents.

With these considerations in mind, for CPA, the thermal bus consisted of 225 0.25 mm bare copper wires cleaned with vinegar ($\sim 10\%$ acetic acid), and packed into the salt pill housing (SPH). A thermal link was made by pressing the 225 wires together with a 1 mm diameter copper wire using a hydraulic crimping tool. The larger wire then extended to the other stages. Using many thin copper wires in this way maximises surface area for crystal growth, and maintains good thermal conductivity whilst minimising eddy currents.

2.2.3 Crystal growth

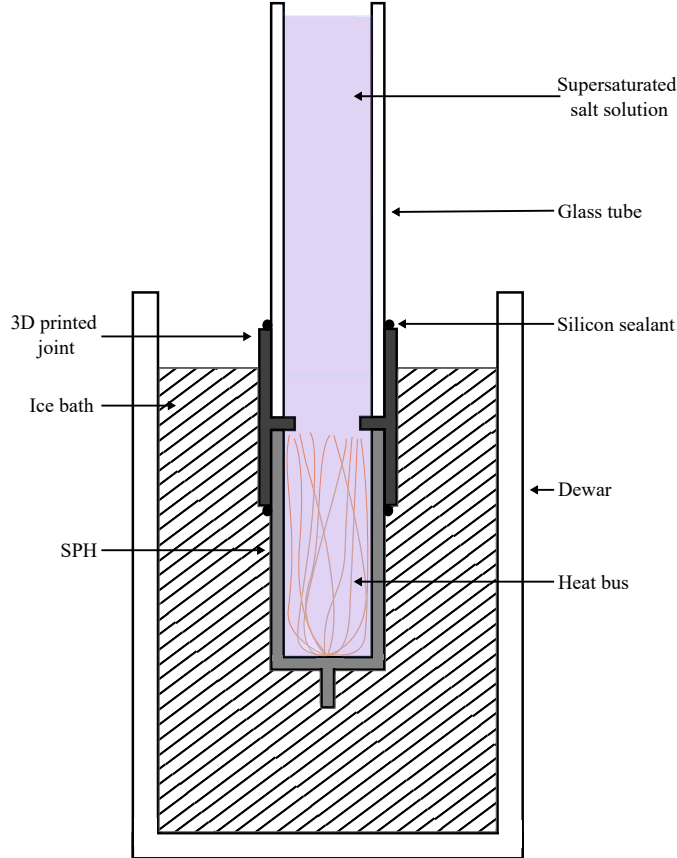


Figure 6: Schematic diagram of crystal growth setup.

For this project, a pre-constructed FAA pill was available. It was decided to construct an additional CPA pill and compare the performances.

The alums can either be grown directly onto the thermal bus, or grown in a separate vessel and packed into the SPH with some high thermal conductivity mater (e.g. Dow Corning grease). The former method is preferable for two reasons. Firstly, the thermal conductivity is significantly greater due to the improved surface contact area. This is particularly important due to the high boundary resistance between salt crystals [23], compared with the internal crystal conductivity. Secondly, a far higher packing density can be achieved by growing the crystals directly onto the bus, increasing the number of moles of paramagnetic material, thus increasing the heat capacity (hence hold time).

A supersaturated solution of CPA was prepared with distilled water using a ratio of 26.44 : 100 of CPA : water at 50°C. Following successful initial tests in a beaker, an apparatus was set up as in fig. 6. The open-topped SPH is sealed to a Pyrex tube using a 3D printed adapter and silicon sealant. The apparatus was cleaned with distilled water to ensure the majority of nucleation would occur on the thermal bus, whilst also serving as a leak check. The pill was kept in an ice bath and the apparatus filled with the hot solution. The solution was then left for 72 hours for crystals to grow. Despite no initial leaks being observed, the majority of the solution leaked out through the 3D-printed polymer connector over time, and very few crystals were formed.

Following this, the simple packing method was employed. 20 g of CPA were packed in using a ratio of 5:1 of CPA : grease, achieving a packing density of 53%.

2.2.4 Pill housing

The SPH was constructed out of stainless steel, as shown in fig. 23. Stainless steel was selected for its easy manufacturability, low cost, and relatively low electrical and thermal conductivities. Following crystal growth, the SPH was sealed using LOCTITE 2850FT stycast.

2.2.5 Future work

Unfortunately, due to time constraints, it was not possible to test the CPA pill, and all further experiments are carried out using FAA. To improve on the method presented here, a stainless steel, instead of 3D printed polymer connecting joint should be used to prevent leaking. Additionally, a slower growth rate should be used. One successful example grew layers of CPA by filling the pill (with thermal bus inside) 1-2ml at a time, every 12–24 hours [18]. Since the SPH volume is 22 ml, this would only take ~1 week.

A further limitation was the relatively low packing density achieved of 53%. Although this would be increased by growing crystals directly onto the thermal bus, an optimised bus design would also be beneficial. The most efficient designs involve a grid of fine wires, spaced 1.2 mm apart, to maximise crystal growth [23]. This could be implemented fairly simply by embedding the wires into a detachable cap on one end of the SPH, with corresponding holes on the other end.

3 Gas-gap heat switch

The heat switch in an ADR system is responsible for thermally isolating and connecting the salt pill from the heat bath. An off-state with low thermal conductivity is essential to provide adiabatic conditions during demagnetisation. Meanwhile, an on-state with high thermal conductivity is necessary for reasonable cycling time. The ratio of the two states is thus a key criterion for the efficacy of an ADR. For the purposes of this project, the requirement is to thermally isolate a ~ 0.1 K salt pill from a ~ 1.5 K heat bath, whilst maintaining cheap, simple and reliable construction.

A variety of switching mechanisms are available, including mechanical, magnetoresistive, gas-gap and superconducting. For this project, a ${}^4\text{He}$ gas-gap heat switch (GGHS) was constructed and tested. This section will present the theory, experimental details and discuss the results and future direction.

3.1 Background

A form of gas heat switch was used in the first ADR designs [24]. These were operated by pumping helium gas into and out of a vacuum chamber surrounding the salt pill. The thermal conductivity between these two states could change by more than two orders of magnitude, from $\sim 0.1 - 10$ mW/K [5]. A simplified setup consists of two plates separated by a gap, with gas between for thermal conductance in the on-state, or a vacuum in the off-state. The gas can be pumped in or out using a sorption pump.

3.1.1 Thermal conductivity

In the on-state of a GGHS, the helium gas dominates the thermal conduction. The rate of heat flow \dot{Q} passing through constant area A , length, l , with a temperature differential dT between temperatures T_1 and T_2 is given by Fourier's law

$$\dot{Q} = -\frac{A}{l} \int_{T_1}^{T_2} \kappa(T) dT, \quad (16)$$

where $\kappa(T)$ is the thermal conductivity of the conducting material. For gases, this value changes depending on the regime of the gas, which is determined by the magnitude of the mean free path, λ , with respect to the gap width, δ , where

$$\lambda = \frac{1}{\sqrt{2\pi d^2 n}}, \quad (17)$$

n is the gas density and d is the molecular diameter [25]. For $\lambda \ll \delta$, at relatively high pressures, the gas enters the molecular regime, where the conductivity is determined by particle collisions and is given by

$$\kappa(T) = \frac{f}{3d^2} \sqrt{\frac{k_B^3 T}{\pi^3 m}}, \quad (18)$$

where f is the degrees of freedom and m is the mass of a molecule. In this regime, the conductivity is independent of pressure, and only needs to be above some threshold. For ${}^3\text{He}$ at 1 K, this corresponds to a minimum pressure of 15 Pa, or 4.5kPa at room temperature (using the ideal gas law) [26]. At this point, $\lambda \approx \delta$, and gas molecules rarely interact with each other, travelling ballistically between the hot and cold plates. In this regime, the conductivity becomes pressure dependent,

$$\kappa = \frac{f}{6} k_B n v \delta \quad (19)$$

where v is the mean speed of the gas molecule [27]. Thus, varying the pressure of the conducting gas between these two regimes can be used to switch the thermal conductivity between high and low. The other significant conduction effect is through the walls of the switch. This dominates when the gas is in the molecular regime or off-state, and can be approximated using eq. (16).

Material	Composition (wt.%)	$\kappa \text{ WK}^{-1}\text{m}^{-1}$	$\rho \Omega \text{ m}^{-1}$
Copper	Cu >99 (RRR \approx 100)	130 [5]	2×10^{-10} [28]
304 SS	Fe 70, Cr 19, Ni 11	0.2 [29]	4.85×10^{-10} [30]
Brass	Cu 70, Zn 30	1.7 [29]	3.25×10^{-8} [31]
Silver	Ag 99.99 (RRR \approx 200)	350 [5]	7×10^{-10} [32]
G10	Fibreglass cloth, epoxy	0.06 [29]	-

Table 3: Properties of commonly used materials in this project. All properties given at 1 K.

3.1.2 Adsorption pump

To vary the pressure so that λ is either \ll or $\gg \delta$, a simple and compact solution is to use a sorption pump composed of a high surface area material, such as activated carbon (with up to $\sim 1000 \text{ m}^2/\text{g}$ surface area [33]). At temperatures below the condensation temperature of the gas, the gas molecules adhere to the surface via Van der Waals forces, forming a thin film [34]. This reduces the pressure in the switch, so the gas enters the molecular regime, and the switch is in the off-state. Upon heating the adsorbent (typically to 15–20 K [35]), the gas is released, transitioning the gas in the gap to the viscous regime, and the switch is turned on.

The amount of helium adsorbed by a mass of activated charcoal can be described by adsorption isotherms, which describe the relationship between the pressure, and the quantity of gas adsorbed at a constant temperature, taking into account the surface area and pore structure of the activated charcoal. Activated charcoal at 1 K is best characterised by Langmuir isotherms, which describe a monolayer of gas adsorbed onto a micropore-structured surface [36]. Using this approach, and the isotherms found in [37], it was estimated that only $\sim 2 \text{ mg}$ of activated charcoal was required for the GGHS used in this project. It is important to note, however, that without further information on the specific surface area, and pore structure of the sample in use, this approach can only serve as a first approximation. A more rigorous approach would be to perform a preliminary adsorption experiment and compare this with the predicted isotherms [38]. As such, the value of 2 mg can only serve as a rough order of magnitude reference point.

Due to this approximative approach and lack of time to iterate, it was decided to opt for an excess amount. The actual mass used was 60 mg. Using an excessive amount of adsorbent has the benefit of increasing pumping speed and guaranteeing adsorption, but has the drawback of increasing desorption temperature [8]. This operating temperature can represent a significant heating contribution to the system, and care must be taken to thermally isolate the getter chamber from the rest of the ADR.

3.1.3 Gas choice

The gas used in a GGHS operating at temperatures below 10 K is typically ${}^3\text{He}$ or ${}^4\text{He}$. Although significantly more expensive, ${}^3\text{He}$ is the standard choice as it has higher gaseous thermal conductivity [39] and condenses to a superfluid far below the switch operating temperature ($T_\lambda \approx 2 \text{ mK}$ [40]).

Conversely, ${}^4\text{He}$ condenses into a superfluid state at $\sim 2.17 \text{ K}$ [41], upon which point it forms a thin film on the interior of the switch, and its thermal conductivity becomes theoretically infinite [5]. While this property may be beneficial for on-state thermal coupling, it represents significant challenges and cannot functionally be operated by a getter. In its superfluid state, the ${}^4\text{He}$ would attempt to form a film over the entire surface area of the system, however, due to the large surface area of the activated carbon, it is unlikely to be able to do this. This means a film will only be formed on the most energetically favourable areas, for example, areas of lowest temperature or highest surface energy [42], increasing the required heat input for desorption.

An alternative approach would be to operate the switch by varying the temperature of the ${}^4\text{He}$ above/below T_λ . For $T < T_\lambda$, a superfluid film would provide high thermal conductivity, and for $T > T_\lambda$, the ${}^4\text{He}$ would be gaseous, and have very low thermal conductivity. However, this would require even heating of the system to above 2.2 K, introducing a large heat input to the ADR.

3.1.4 Design

In the interest of simplicity, a design was chosen that consists of two plates separated by a narrow gas gap. Brass was chosen as the material for these plates as it has high thermal conductivity, lower electrical conductivity than copper, and is easily machinable (see table 3).

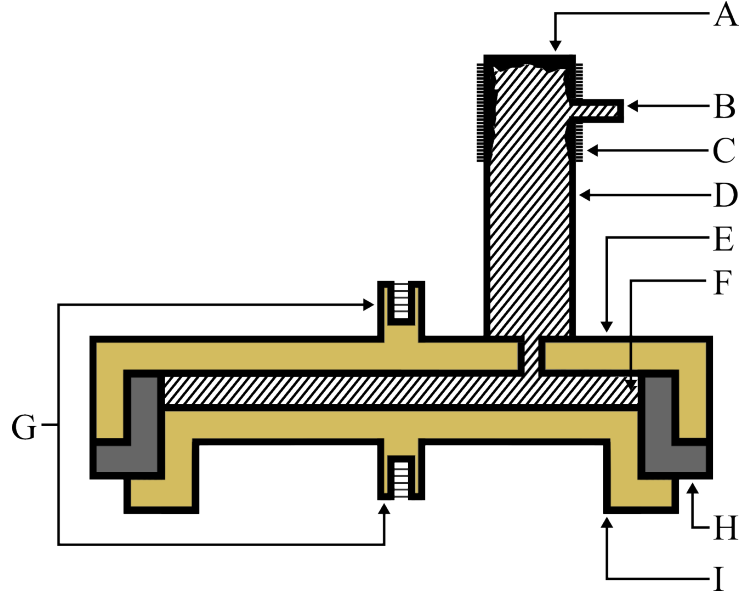


Figure 7: Schematic diagram of GGHS (not to scale). The shaded region represents the gas (in the on-state), the yellow section brass, the dark grey section steel. (A) Activated charcoal powder; (B) capillary fill tube; (C) Constantan heater; (D) getter enclosure; (E) switch top plate; (F) gas gap ($50 \mu\text{m}$); (G) M3 screw holes for thermal link; (H) steel spacer; (I) switch bottom plate.

To achieve sufficient on-state conductance for a reasonable cycle time, the ratio A/l of the brass plates (E, I, fig. 7) can be maximised, within the constraints of the vacuum cannister. This has the added benefit of reducing the off-state conductance by increasing the amount of material the heat current must flow through. Fixing the gas-gap at the minimum machinable distance of $\sim 50 \mu\text{m}$, the effect of different plate areas on the time to reach equilibrium during magnetisation (step II in section 1.1.1) can be modelled fig. 8.

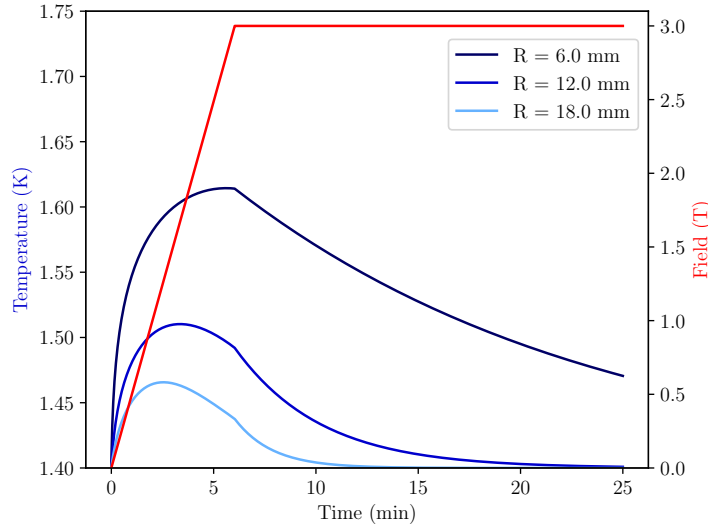
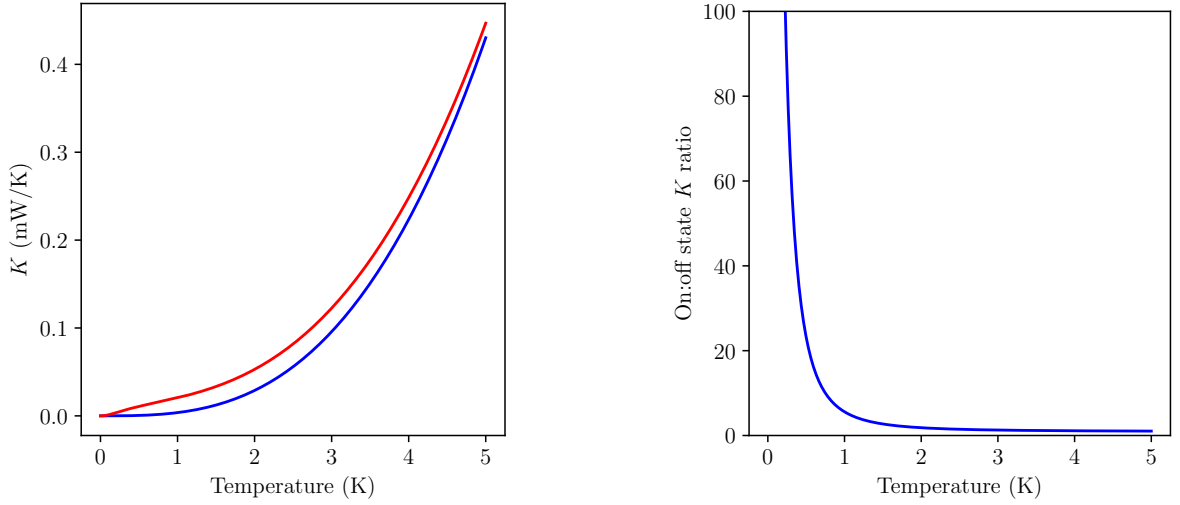


Figure 8: The effect of various plate radii on the time taken to equilibrate to 1.4K, following magnetisation to 3T for 0.04 moles FAA, GGHS. The actual value used in construction was $R = 12 \text{ mm}$. Temperatures are shown in blue, magnetic field in red.

To obtain a low thermal conductance in the off-state, a steel spacer was used to separate the plates. By treating the brass-steel-brass wall as elements in series, an approximation for the total heat current can be found in the off-state using eq. (16). To model the on-state heat flow, a similar approach is employed, with brass- ${}^4\text{He}$ -brass elements, using eq. (18) for the conductivity of ${}^4\text{He}$. This model predicts an off-state

thermal conductance of 0.003 W/K, and an on : off ratio of 6.5:1 at 1 K (see fig. 8).



(a) Estimated GGHS thermal conductance in on and off-states using data from table 4.

(b) Ratio of on:off state thermal conductance for the GGHS.

Figure 9: Predicted on and off-state thermal conductance of the GGHS.

For the design of the getter enclosure, care needs to be taken to minimise the heat load on the pill, and maintain T_b . Once more using eq. (16), this can be ensured by using a low thermal conductivity material, and using a geometry with sufficiently low A/l . Employing steel for reasons previously discussed (see section 2.2.4), the necessary value for A/l can be determined by equating eq. (16) to the cooling power of the 1 K pot. This value varies significantly depending on the specific pumping rate of the 1 K pot, but for the equipment available for this project, a reasonable value was taken to be $Q_{\text{pot}} \approx 10$ mW. Using a required desorption temperature of 25 K ($\sim 100\%$ higher than the typical range [35]), the maximum operable A/l would be 2.7 mm at 1.5K. Based on this, and in the interest of simplicity, a single steel tube was machined (D, fig. 10), with an A/l as measured between the getter and switch of 0.6 mm.

3.1.5 Experimental methods

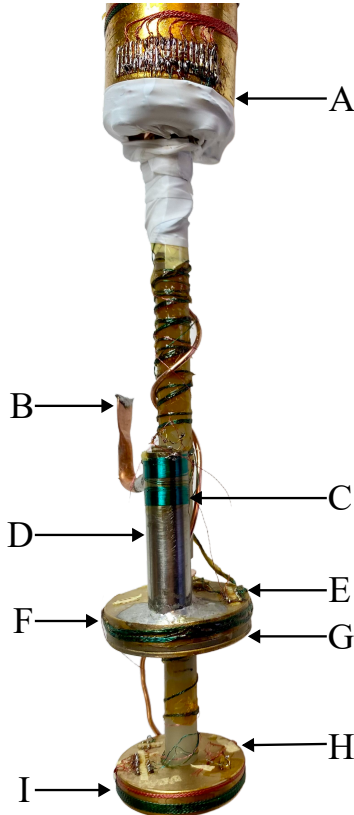


Figure 10: Experimental setup for GGHS testing. (A) 1 K pot; (B) sealed fill line; (C) getter heater; (D) getter enclosure; (E) GGHS top plate; (F) GGHS heater; (G) GGHS bottom plate; (H) experimental stage; (I) experimental stage heater.

To assemble the sorption pump, activated carbon was glued to the interior of a steel enclosure and affixed to the top plate of the GGHS. A 0.08 mm Constantan wire was wound around the enclosure to supply heat to operate the getter. The switch was then filled via the fill tube (B, fig. 10) with 50 kPa ${}^4\text{He}$ (1.34×10^{-8} moles) at room temperature, corresponding to $\sim 170\text{Pa}$ at 4 K, and sealed using a mechanical crimping tool and solder. ${}^4\text{He}$, being significantly less expensive than ${}^3\text{He}$, was used as a preliminary test to assess the getter operation at 4K (i.e. $T > T_\lambda$).

With the switch assembled, a preliminary test was performed to assess the switch performance. Key performance parameters were the power input required to desorb the gas, the temperature at the switch, and the on and off-state thermal conductance. 12 mW was input to the experimental stage (H, I fig. 10), warming it to a steady 7.25 K, and setting up a temperature gradient across the GGHS. This would allow the off-state thermal conductance to be determined, as well as any variations as the getter is warmed. Following this, the power input to warm the getter was incrementally increased and the temperature of the stage, heat switch and getter recorded. This was repeated several times for various enclosure temperature ranges, in order to determine the temperature required to desorb the ${}^4\text{He}$. All temperature measurements were taken using Cernox (CX-1030D-SD) chip resistors in a 4-wire configuration located on the carbon enclosure, top plate of the GGHS, and experimental stage.

Component	Material	Dimensions (mm)	Conductance (vertically) (W/K) (1 K)
Carbon enclosure	Steel	R (inner) = 3.5 R (outer) = 4 l = 30	3.9×10^{-5}
Switch top plate	Brass	R = 13 l = 1	0.53
Switch bottom plate	Brass	R = 12 l = 1	0.45
Top plate wall	Brass	R (inner) = 13 R (outer) = 14 l = 4	0.021
Bottom plate wall (vert)	Brass	R (inner) = 11 R (outer) = 12 l = 4	0.018
Steel spacer (vert)	Steel	R (inner) = 12 R (outer) = 13 l = 3	0.0026

Table 4: Relevant parameters of GGHS experimental set up. Thermal conductance serves only as approximation using eq. (16), with, κ from table 3.

3.1.6 Results

Using the data collected in fig. 11, the temperature-dependent GGHS off-state thermal conductivity was calculated (fig. 12), with a value at 4.5 K of $K_{\text{off}} = 0.38 \pm 0.0040$ mW/K. As can be seen from the inset in fig. 11, this off-state is reproducibly established following heating and cooling back to 4 K. The error on the Cernox resistors for $T_{\text{stage}} - T_{\text{switch}}$ was propagated by calculating the square-root of the sum of the variance of each at constant 4 K. The magnetoresistance of the resistors was not factored in to the error (see fig. 48). To calculate the power input, the constant resistance of the heater at 4 K was used with the applied voltage.

The raw temperature data for determining the desorption temperature is shown in fig. 13. The approach was to do an initial large temperature range sweep, then further investigate regions of interest. From the data in fig. 13a, this was judged to be ≥ 30 K. As more heat is input at the getter, the temperature recordings at the switch became highly variable. The standard deviation at 61 K is $100 \times$ the value at 4 K (see appendix A). A moving 20-point mean was taken to smooth the results. The error on the total thermal conductance, K , was then propagated as before.

Figure 14 and fig. 15 show the variance of the switch conductance with varying getter temperature, and at constant getter temperature at 30.50 ± 0.04 K, respectively. Both plots feature plateaus in K , which are featured in the insets. From these plateaus, a mean K can be calculated, yielding $K = 20.02 \pm 1.04$ (mW/K) at a getter temperature of 61.01 ± 0.04 , and $K = 10.36 \pm 1.17$ (mW/K) at 30.50 ± 0.04 K.

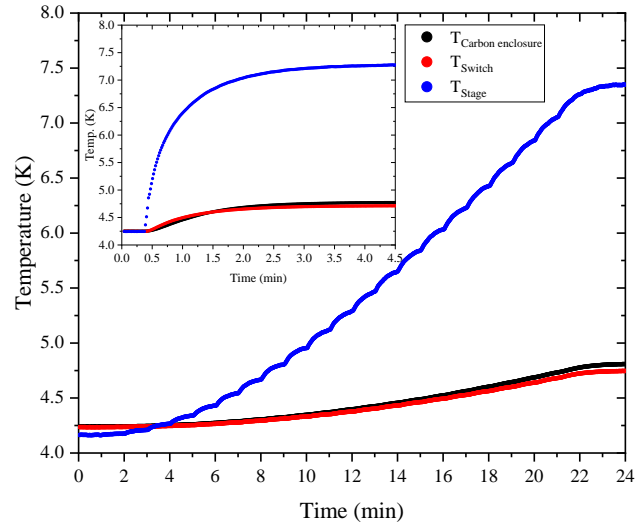


Figure 11: Temperature variation of stage, switch and carbon enclosure with the GGHS in the off-state, with increasing heat input at the stage. Used to calculate the off-state thermal conductivity. Inset shows a reproducible steady plateau following cooling and re-heating.

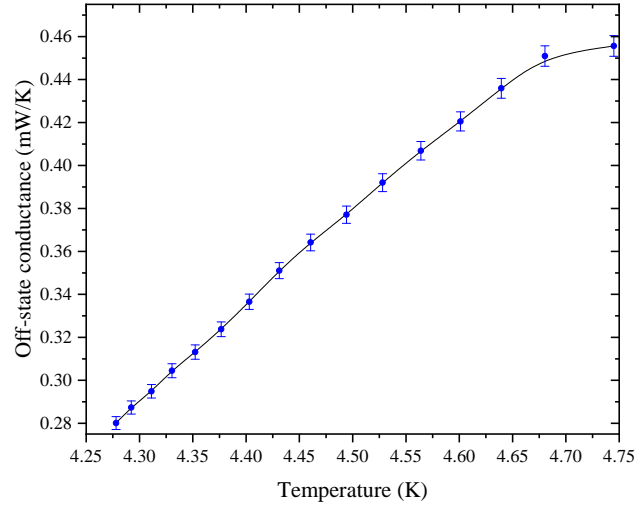
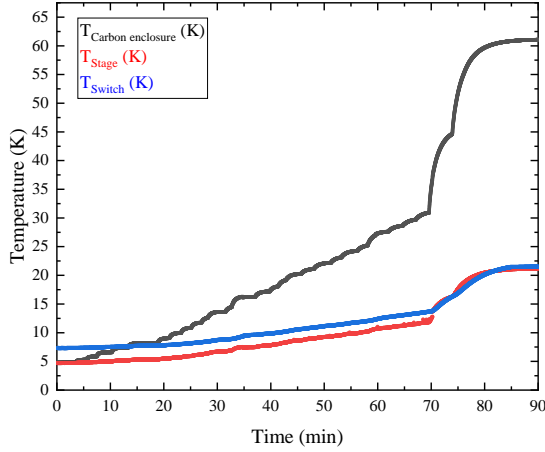
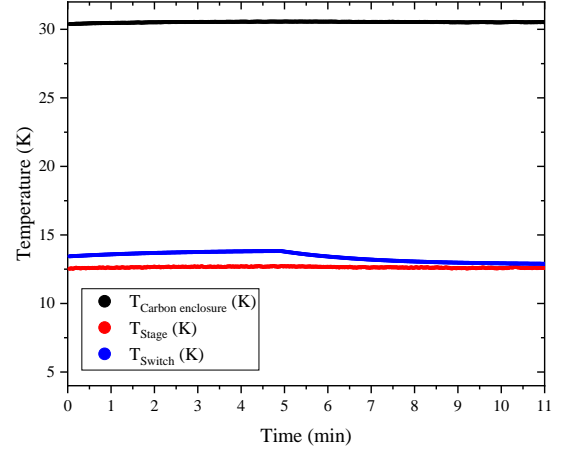


Figure 12: Off-state thermal conductivity of the GGHS. Calculated from fig. 11.



(a) Initial ‘sweep’, varying temperature from 5-60 K.



(b) Variation of GGHS and ES temperatures when held at a constant temperature of 30.50 ± 0.04 K.

Figure 13: Raw temperature data from experiment to determine the desorption temperature of ${}^4\text{He}$.

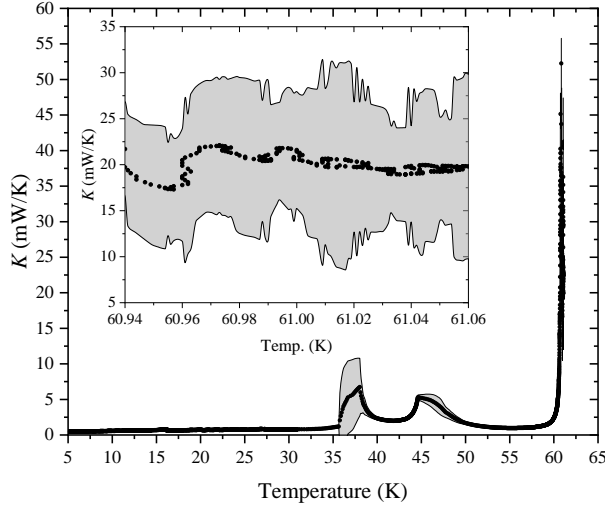


Figure 14: The variation of thermal conductance of the GGHS with increased getter temperature. The inset shows a plateau at a temperature of 61.01 ± 0.04 K.

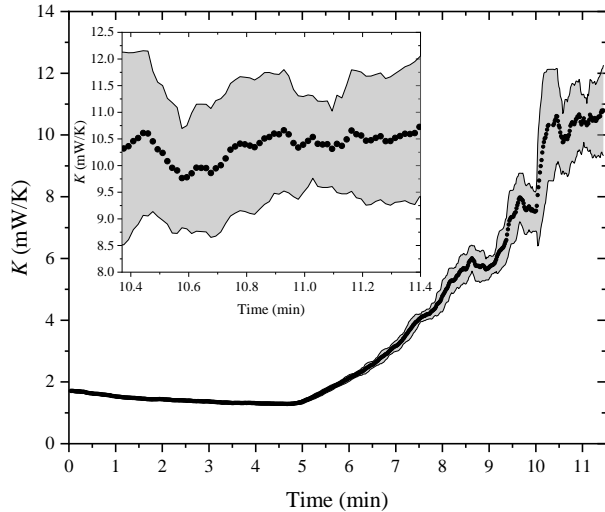


Figure 15: The variation of K with time at a constant getter temperature of 30.50 ± 0.04 K.

3.1.7 Discussion

The off-state thermal conductance achieved of $K_{\text{off}} = 0.38 \pm 0.0040 \text{ mW/K}$ at $4.50 \pm 0.02 \text{ K}$ is comparable with other systems in this temperature region [26], and only 3.5% different from the value of 0.367 mW/K at 4.6 K estimated by the model (fig. 9a). Thus, if the model's accuracy is sustained at lower temperatures, at 0.5 K , the on : off K ratio would be 25, and the off-state $K = 4.65 \times 10^{-4} \text{ mW/K}$.

It is important to note that these K values include the thermal conduction through the linking copper and brass experimental stage between the heat switch and the stage thermometer, thus the values achieved are not representative of the conductivity of the switch itself.

From the rapid increase in K in fig. 14 and fig. 15, it is implied that there is a transition from the molecular regime to the viscous regime, meaning the ^4He has been desorbed, and the on-state activated. This is supported by the fact that in both cases, a plateau is achieved, where a constant volume of gas has been desorbed into the switch, and constant K established. The temperature at which this occurs cannot be stated with confidence. From fig. 13a and fig. 14, it would initially appear that desorption only occurs at $\sim 60 \text{ K}$. Upon further investigation at $\sim 30 \text{ K}$, it appears that an on-state is, in fact, achieved following a longer hold time at this temperature. Using the conductances at a getter temperature of 4.2 K and 30 K , an on : off ratio of 27.3 was achieved.

However, at a temperature of $30.50 \pm 0.04 \text{ K}$, the experimental stage temperature is increased by $\sim 5.5 \text{ K}$ once equilibrium has been reached. For ADR operation with the goal of cooling to $\sim 0.1 \text{ K}$, this heat input is prohibitively large, and switch operation would negate any cooling effect. For this reason, this iteration of the GGHS is inoperable.

The causes of this failure can be simply described by eq. (16). Firstly, by stating ΔT as the difference in temperature of the switch and the getter, it can be seen that the unusually high desorption temperature increased the heat load on the stage, by approximately a factor of 2 compared to expected desorption temperatures. This is most likely the result of excessive quantity of getter used. Secondly, the cooling power of the 1 K pot was of the order of 1 mW . This is a factor of 10-30 times less than anticipated, and with sufficient time for preparation, this quantity would have been determined prior to switch construction. The most significant factor, however, is that despite being an order of magnitude below the expected requirements, in practice, the conductance of the link between the getter and the switch (i.e. the lower $3/4$ of the getter chamber, see fig. 10) was too high. To reduce the heat load of the getter heater to $< 1 \text{ mW}$, and assuming steel was still used, a value of A/l of $\leq 0.17 \text{ mm}$ would be required, compared with the value of 0.5 mm employed.

With these factors taken into account, a second iteration was constructed fig. 16. Here, $A/l = 0.09 \text{ mm}$, and brass is used for the getter chamber instead of steel to improve the conductance from the heater to the getter, reducing the required power input. Also, the thickness of the steel spacer was increased by a factor of three to reduce off-state conductivity. Finally, only 10 mg of activated charcoal was used to reduce the heat of desorption. Unfortunately, due to the time constraints on this project, it could not be tested.

Another direction for improvement could be to implement a passive GGHS, which alternates between the on and off-states with the change in temperature due to magnetisation/demagnetisation of the salt, removing the requirement for an external heat input [43].

3.2 Conclusions

A GGHS was constructed using ^4He , achieving an off-state conductance of $K_{\text{off}} = 0.38 \pm 0.0040 \text{ mW/K}$ at $4.50 \pm 0.02 \text{ K}$, and an on state $K_{\text{on}} = 10.36 \pm 1.17 \text{ (mW/K)}$ at $30.50 \pm 0.04 \text{ K}$, yielding an on : off ratio of 27.3. The power input required to desorb the gas in this design was, however, prohibitively large for ADR implementation. Due to the successful switching into the on and off-states, and properties of GGHS of high levels of control over the switching and low off-state, with iteration, it can be concluded that a GGHS could be implemented in a practical, cost-effective way for ADR.

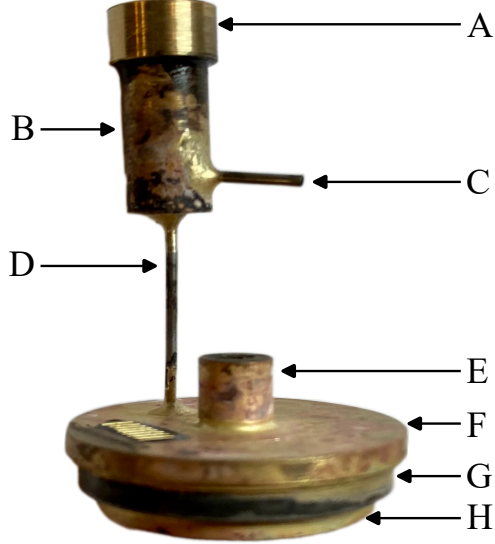


Figure 16: Second iteration of the GGHS.(A) getter enclosure cap, affixed with Stycast; (B) brass getter enclosure; (C) capillary fill tube; (D) capillary gas tube; (E) M3 screw hole for thermal link; (F) GGHS top plate; (G) steel spacer; (H) GGHS bottom plate.

4 Refrigeration

This section presents the design process, experimental details and performance of the ADR constructed as the main goal of this project.

4.1 Design

Following the failure of the GGHS, the simplest alternative is to implement a superconducting heat switch. For this project, a conventional, type I, lead heat switch was implemented, as well as a less conventional type II niobium heat switch.

4.1.1 Lead heat switch

Type I superconducting heat switches operate via the property that in the superconducting state, as electrons condense into Cooper pairs, the number available for conduction decreases as $\exp(-\Delta E/k_B T)$ (where Δ is the energy gap) [44]. Thus, the conduction becomes phonon dominated, and extremely low as $T \rightarrow 0$. This provides the off-state of the switch. By applying an external field greater than the critical field, H_c of the material, the superconducting state is destroyed, and the material is normally conducting, so the switch is in the on-state.

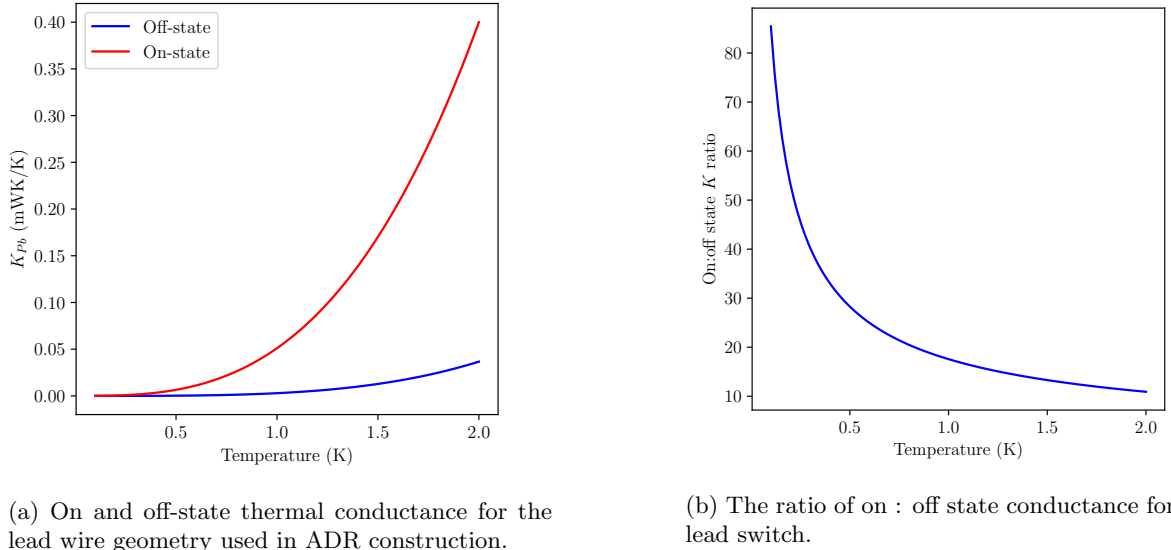
To achieve sufficiently low thermal conductivity in the off state, superconducting heat switches are generally required to operate $< 0.1T_c$. This project aims to cool from a ~ 1.5 K bath, which means the commonly used type I superconductors (see table 5) cannot operate below this threshold for the duration of demagnetisation. Lead, however, has the highest T_c and H_c , so can be used to achieve the best switching ratio.

Material	T_c (K)	H_c (mT)
Aluminium	1.2	10.5
Indium	3.4	29.3
Tin	3.7	30.9
Lead	7.2	80.3

Table 5: Properties of available superconducting materials. Adapted from [45].

To simplify the construction and reduce cost, the switch will be operated by the same superconducting magnet that drives the refrigeration. This has the drawback of reducing the control over the point at

which the switch is activated. To limit this, the superconducting switch can be displaced from the field centre axially, in Z (see fig. 18). By displacing the switch 10 cm from the pill, the field strength at the switch is only a third that of the field at the pill centre, effectively tripling the time spent in the off-state during demagnetisation.



(a) On and off-state thermal conductance for the lead wire geometry used in ADR construction.

(b) The ratio of on : off state conductance for the lead switch.

Figure 17: Estimated thermal conductance for the lead switch used in ADR construction. Modelled using eq. (21).

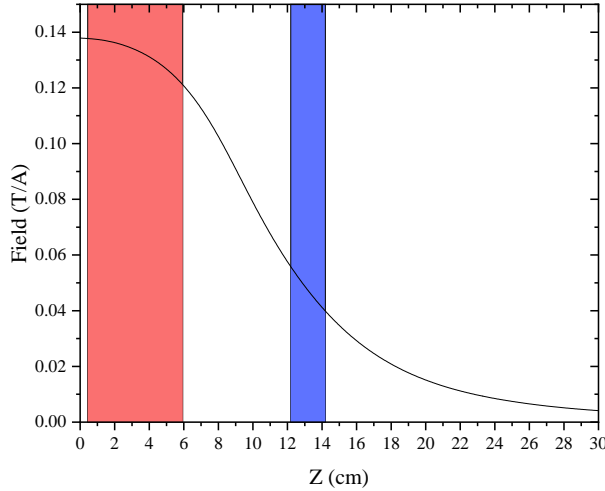


Figure 18: 1 ampere field profile for the NbSn/NbTi superconducting magnet used for all experiments. The blue region represents the Z region occupied by the pill, the red region the coiled superconducting heat switch.

4.1.2 Niobium heat switch

Despite often having significantly higher T_c , historically, type II superconductors have rarely been used as heat switches. This is due to the fact that unlike type I superconductors, they have an intermediate mixed state where magnetic fields can penetrate. This means they have a lower, H_{c1} , and upper, H_{c2} , critical field where in general for a pure sample, the magnitude of the latter follows the relation

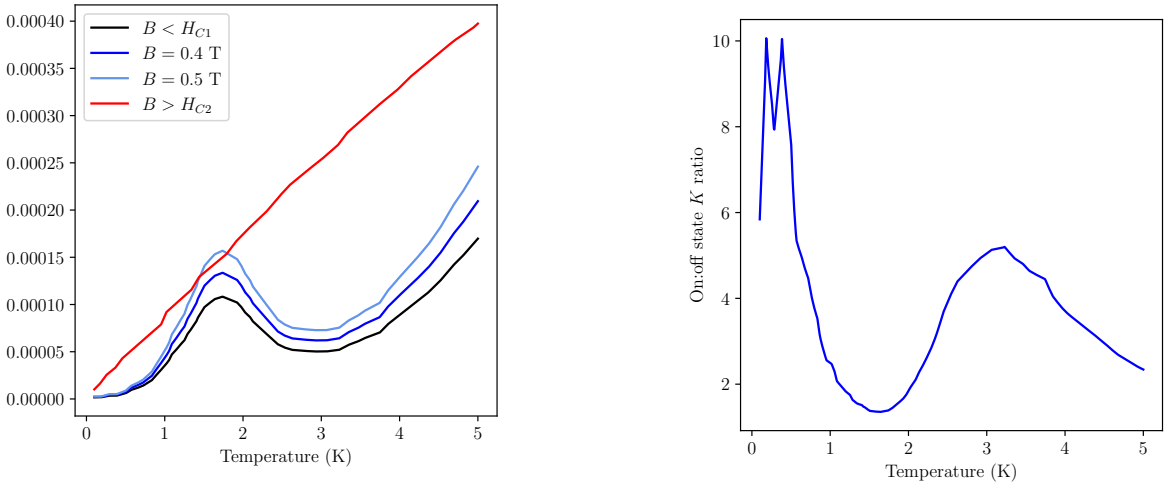
$$H_{c2} \propto T_c^2, \quad (20)$$

meaning, the applied field to destroy the superconducting state is often prohibitively large for switch operation. Niobium, however, is only weakly type II and $H_{c2} \simeq 2H_{c1}$ [46], resulting in a steeper super-

conducting transition, and a critical field that is easily reached in a lab environment. The magnitude of both H_{c1} and H_{c2} is RRR dependent; for example, for a sample with an RRR of 400, $H_{c1} = 170$ mT, $H_{c2} = 400$ mT, whilst for RRR = 246, $H_{c1} = 280$ mT, and $H_{c2} = 580$ mT [47]. This cannot be accurately extrapolated to other samples, but gives an indication of the relationship.

Another complication with using type II superconductors is the phonon bump. This occurs as more electrons condense into Cooper pairs, reducing the electron-phonon scattering cross-section, which can lead to an increase in thermal conductivity in a narrow temperature range. This, too, is RRR dependent, with lower RRR samples exhibiting a larger ‘bump’, thus a larger heat leak (see fig. 19a) [48, 49].

The effects of these two opposing RRR-dependent properties must be balanced by carefully selecting the purity of a sample to optimise its efficacy as a heat switch.



(a) On and off-state thermal conductance for the lead wire geometry used in ADR construction. Note the phonon ‘bump’ at $\sim 1\text{-}2$ K.

(b) The ratio of on : off state conductance for the lead switch.

Figure 19: Estimated thermal conductance for the niobium heat switch used in ADR construction. Interpolated from [48], for RRR = 192.

4.1.3 Design model

Design decisions could be motivated at a high level by the considerations discussed so far, but to better optimise the design, a mathematical model was made. An approximation model consisted of the cooling due to demagnetisation, with a free-ion paramagnetic salt connected to a 1.5 K bath by a lead heat switch. By using the definition of the specific heat capacity eq. (3), and by differentiating eq. (5), the change in temperature due to demagnetisation can be calculated, along with a heat leak through the switch, given by

$$\kappa(T, B) = \begin{cases} 52T^{2.97} \text{ Wm}^{-1}\text{K}^{-1}, & \text{if } B > 80\text{mT} \\ 2.96T^{3.0569} \text{ Wm}^{-1}\text{K}^{-1}, & \text{if } B \leq 80\text{mT} \end{cases} \quad (21)$$

for $0.01K \leq T \leq 2.85K$ [20]. Using this model, the effect of varying lead wire length could be optimised, taking into account time to equilibrate (stage II, section 1.1.1), and off-state resistance. As a second heat source, the eddy currents generated by the ramping field could be modelled using eq. (15) for various components, materials, and geometries. The cooling power of the ADR is of the order of 0.01-1 mW, so up to a heat leak contribution of $\sim 10^{-7}$ W, the thermal conductivity should be maximised. From this, the materials in table 6 were selected. Another factor, concerning eddy currents, is the rate of demagnetisation. Since $Q_e \propto (dB/dt)^2$ and the total energy leak through the switch is $\propto t$, a balance must be found to find the optimal ramp rate to minimise heat leak.

Component	Material	Q (W) 0.5 (T/min)	Q (W) 0.1 (T/min)
Thermal Links	Cu	2.19×10^{-9}	8.78×10^{-11}
ES	Brass	1.00×10^{-7}	4.01×10^{-9}
SPH	SS 304	5.45×10^{-8}	2.18×10^{-9}
Heat bus	Ag	4.09×10^{-11}	1.64×10^{-12}

Table 6: The estimated heat leak generated by eddy currents in different components.

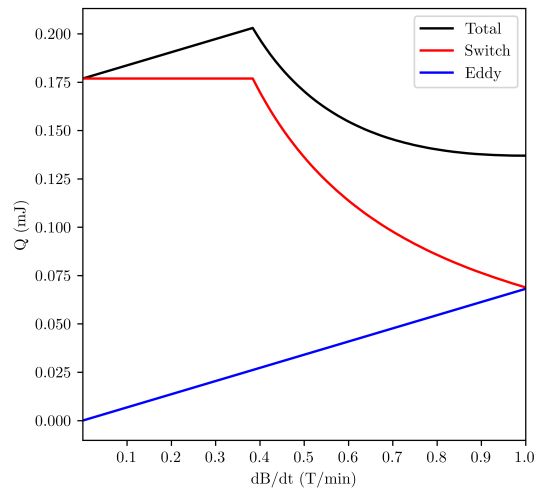
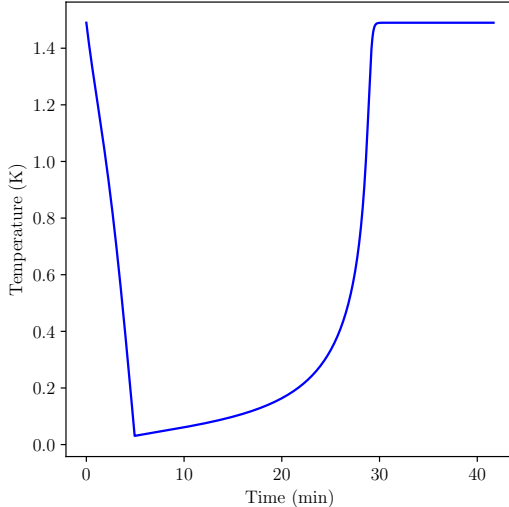


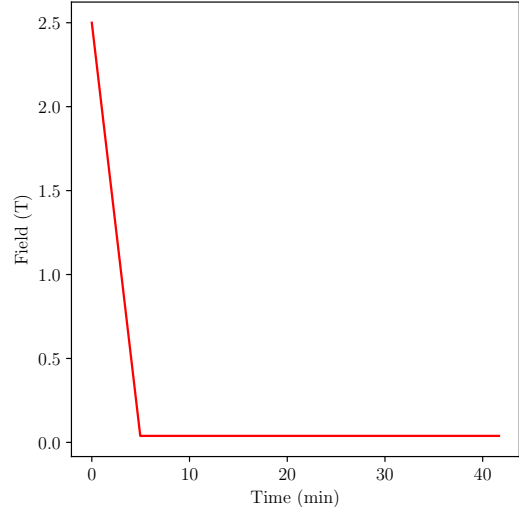
Figure 20: The heat leaks due to the heat switch and eddy currents for a demagnetisation from 2T for various demagnetisation rates, at a constant temperature of 0.9K.

The third significant heat leak considered during the design process was through the support structure. For this, a simple G10 rod was used, owing to its low thermal conductivity and practicality. The heat leak through the G10 can be simply modelled using eq. (16).

Considering these factors, a design model was constructed, enabling the inter-relating design parameters to be varied and their effects observed. The purpose of this was not to be a comprehensive, accurate model, but to observe the impacts of different design choices.



(a) Temperature of salt pill during demagnetisation according to the design model. Minimum temperature = 30 mK.



(b) Applied field on salt pill during demagnetisation according to the design model. $B_i = 2$ (T), $dB/dt = -0.5$ (T/min).

Figure 21: Design model results for a $B_i = 2$ (T), $dB/dt_{\text{demag}} = -0.5$ (T/min) demagnetisation. Specific heat calculated from the free-ion approximation.

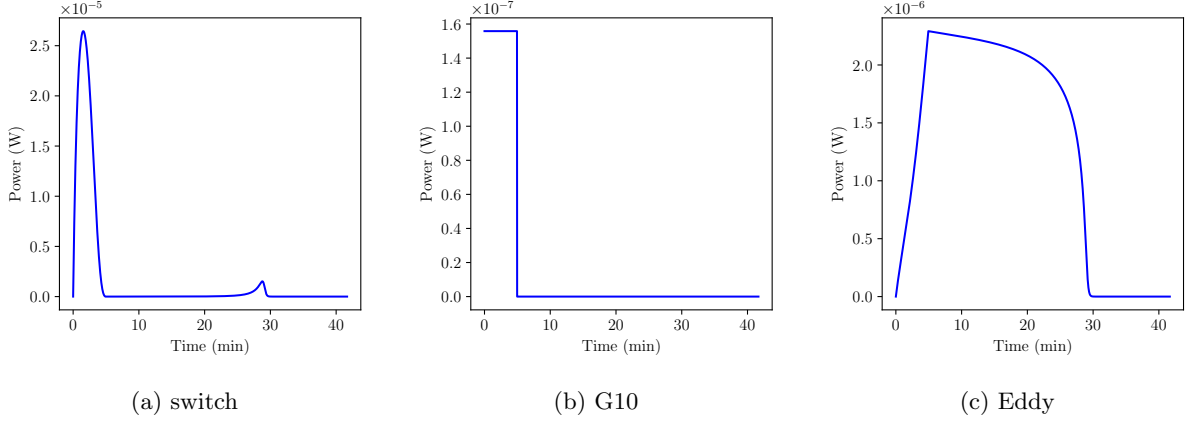


Figure 22: Heat leaks design model.

4.2 Experimental methods

With these key design considerations in mind, the ADR probe could be constructed fig. 4. Temperature data were collected on the ES using a Cernox (CX) and $2.2\text{ k}\Omega$ ruthenium oxide (RO) chip resistor, and on the 1 K pot with a CX, all set up in a 4-wire configuration. The CX resistors were calibrated to 1 K, and the RO to 30 mK. All demagnetisation results were collected with the RO on the ES. All thermometers were connected to the contact pad on the 1 K pot using 0.08 mm twisted pairs of enamelled Constantan. Each wire contributed a negligible heat leak of $\sim 1 \times 10^{-9}\text{ W}$ for a 1 K temperature gradient.

The pill was structurally connected to the 1K pot with a 1 cm G10 rod, and the ES to the pill with a 0.5 cm G10 rod. Thermal contact was established with 1 mm copper wires, crimped at each end and pressed between nuts on a bolt (F fig. 23).

The apparatus was the same for both lead and niobium switches. For the lead switch, 10 cm was wrapped around the top of the G10 rod (10 cm from SPH), and held in place with tape. One end was pressed with a bolt against the 1 K pot, the other to one end of a copper linking wire. This was to ensure the wire was as far from the field centre as possible. For the niobium switch, a piece of 65x0.5x0.3, 99.8% purity foil was used. This was affixed in the same way as lead.

With the probe assembled, a can was placed over the top, and sealed with an indium seal. The can was pumped down to $\sim 10^{-5}$ mBar, meaning conduction through any residual gas is negligible. The probe was then placed within an ${}^4\text{He}$ -cooled NbSn/NbTi superconducting solenoid fig. 18.

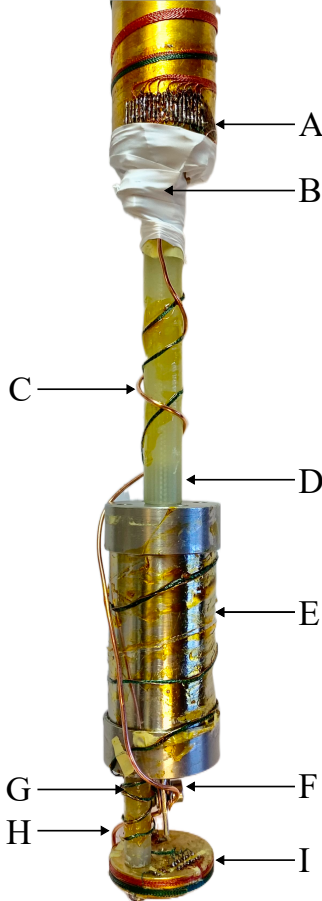


Figure 23: Probe setup used for all demagnetisations. (A) 1 K pot; (B) superconducting heat switch (beneath PTFE tape); (C) thermal link from 1 K to SPH; (D) 1 cm G10 support rod; (E) SPH; (F) stage link to thermal bus; (G) 0.6 cm G10 support rod; (H) thermal link to ES; (I) ES.

4.3 Results

4.3.1 Lead heat switch

For the ADR setup using a lead heat switch, demagnetisation was performed at various initial fields, B_i and demagnetisation rate, dB/dt . The B_i at the centre of the pill is in fact 3% less than the applied field (see fig. 18), so values in appendix C, appendix C are only to 1 s.f. For a demagnetisation rate of 0.5 T/min, the minimum temperature achieved was $T_f = 0.44 \pm 0.02$ K, and $T_f = 0.43 \pm 0.03$ K for 0.1 T/min (see fig. 26).

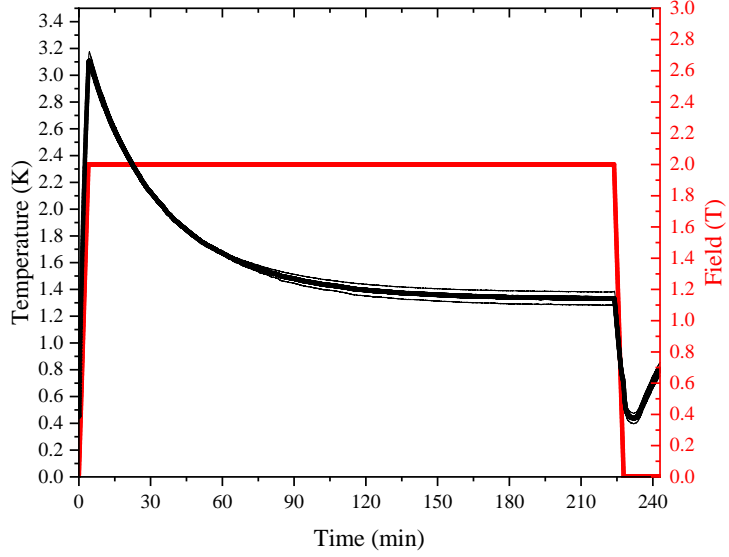
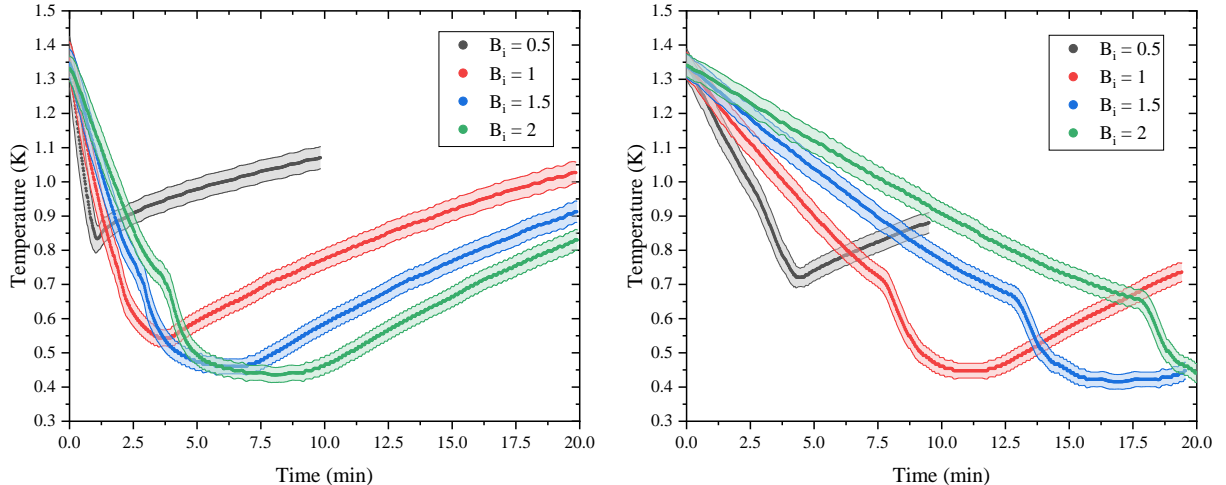


Figure 24: A typical magnetisation/demagnetisation cycle. Here, $B_i = 2$ T, $dB/dt = 0.5$ T/min, $T_i = 1.4$ K, $T_f = 0.44 \pm 0.02$, using a lead heat switch.



(a) The temperature during demagnetisation from various B_i , with $dB/dt = 0.1$ T/min.

(b) The temperature during demagnetisation from various B_i , with $dB/dt = 0.5$ T/min.

Figure 25: Demagnetisation results using a lead heat switch.

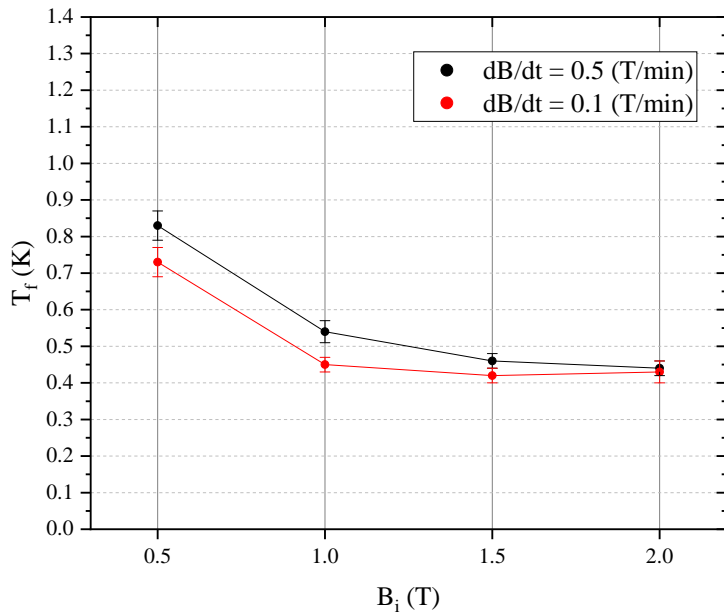


Figure 26: Lead switch demagnetisation runs, final temperature T_f K versus initial field B_i T for $dB/dt = 0.5$ (grey) and 0.1 (red) T/min.

4.3.2 Niobium heat switch

The niobium demagnetisations were carried out at higher initial temperature, at 1.75 and 2.05 K. This was required due to the tight time constraints, and the very long equilibrium time – taking 24 hours to cool from 80 to 4.5 K. They were also carried out at higher field and smaller dB/dt , in an attempt to achieve minimum final temperature, following the lead results, and the expected dS/dB (see fig. 3).

B_i (T)	dB/dt (T/min)	T_i (K)	T_f (K)
3	0.05	1.742 ± 0.005	0.49 ± 0.03
5	0.1	2.040 ± 0.007	0.49 ± 0.03

Table 7: Parameters of the two demagnetisations performed with a niobium heat switch.

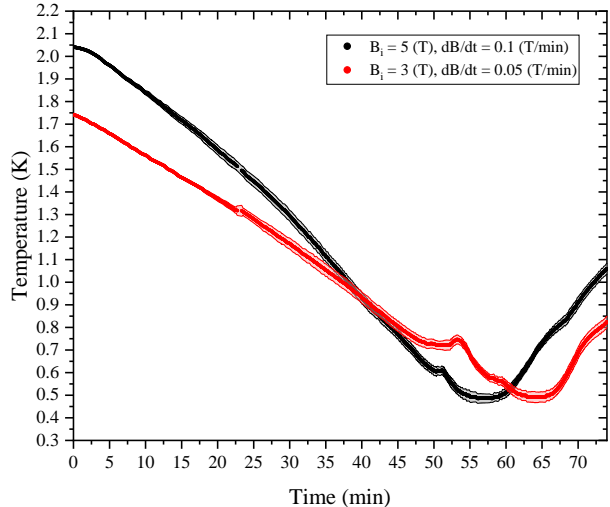


Figure 27: Demagnetisations using niobium heat switch.

4.3.3 Errors

The resistances of the CX thermometers are $\propto \exp(T^{-1/2})$, resulting in very large resistance at low temperatures, meaning they are only accurate down to ~ 1 K. Thus, for the demagnetisations, a RO resistor is used. To calculate the error on the RO temperatures, the difference in recorded temperature is found in the region where the CX is accurate, and extrapolated to the recorded RO temperature points, then, added to the standard deviation on the RO measurements.

4.4 Discussion

4.4.1 ADR performance

The minimum temperature achieved was $T = 0.42 \pm 0.02$ K using a lead heat switch, with $B_i = 1.5$ T, and $dB/dt = -1.5$ T/min. For these parameters, according to the free ion approximation eq. (10), the theoretical minimum temperature is $T = 0.056$ K. Thus, the ADR did not achieve the target temperature of 100 mK, and is still in the range achievable by reducing the vapour pressure of liquid helium.

To assess the performance of the ADR, two different efficiencies are useful; the first of which being the ratio of the change in temperature observed, $T_i - T_f$, to the theoretical maximum change in temperature, $T_i - T_t$. The temperature efficiency, E_T of all demagnetisations, is plotted in fig. 29.

Another useful parameter is the achieved by comparing the heat removed during demagnetisation, with the heat required to be removed to cool to the theoretical minimum temperature, T_t . This can be simply estimated by integrating the specific heat capacity with respect to temperature (see fig. 28), with the limits being the maximum and minimum temperatures. Using the experimental heat capacities for FAA and steel, which dominate the system, the energy removed by demagnetisation is plotted in fig. 31. The energy efficiency, E_Q is provided for all demagnetisations in fig. 29.

It can be seen, then, that as expected, the efficiency was highest for larger B_i , with a consistent E_Q of ~ 0.7 . This plateau is indicative of reduced dT/dM at this temperature (see fig. 3), and the increased heat leaks due to the larger temperature gradient.

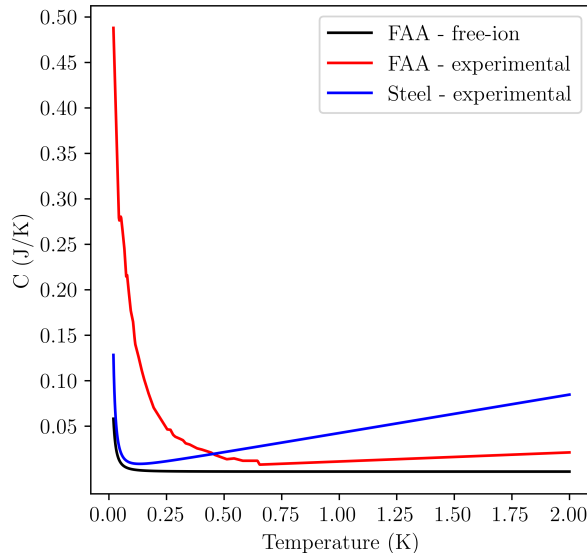


Figure 28: The heat capacities for 0.04 moles FAA and 91g stainless steel, plotted using experimental values from [50] for FAA and [51] for steel. The free-ion zero-field heat capacity is also plotted for FAA.

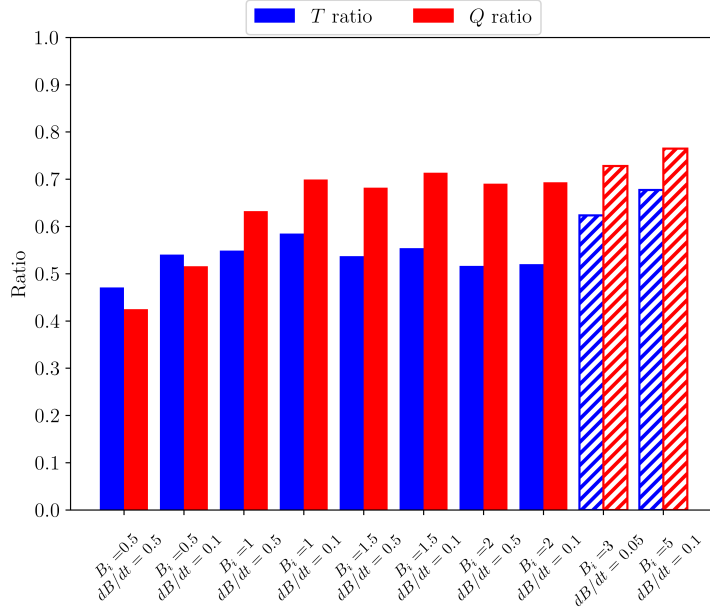


Figure 29: The efficiencies of all demagnetisations given by E_T (blue), and E_Q (red). Solid bars represent lead switch runs, hatched bars represent niobium.

4.4.2 Lead switch performance

The difference between the ideal and achieved demagnetisation energies provides an estimate for the total heat leak, and is plotted in fig. 31. For the lead heat switch, the total heat leak varied from 30-45 mJ. The proportion of this heat leak that can be attributed to the lead switch can be estimated.

From fig. 25, a drastic change in gradient occurs, whereafter the rate of cooling increases. This consistently occurs during demagnetisations at $B \approx 211$ mT, corresponding to $B_{\text{switch}} \approx 74$ mT. This value is comparable to the critical field, $H_c = 80$ mT [20], so can be taken as the superconducting transition for the heat switch.

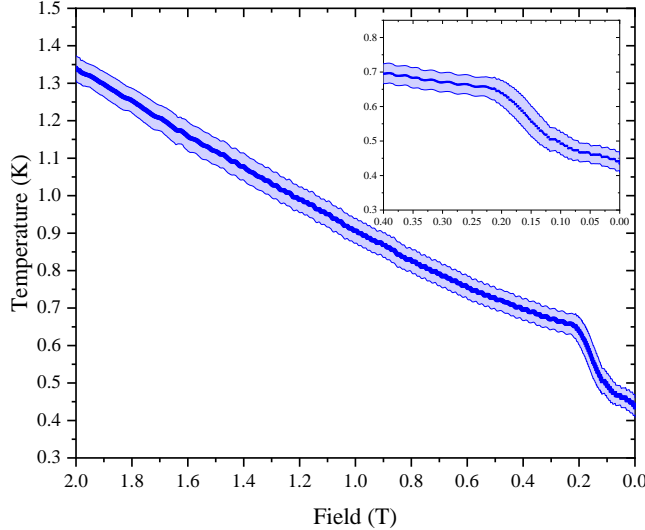


Figure 30: Temperature vs applied field for $B_i = 2$ T, $\frac{dB}{dt} = 0.1$ T/min. The field has been translated so $B = 0$ at T_f , to account for cooling lag. Superconducting transition at $B = 211$ mT.

By considering the dominant heat capacities in the probe (see fig. 28), the transient heating/cooling power can be calculated from the linear dT/dt for each 0.1 T/min demagnetisation in fig. 25b (slower demagnetisation rate has sharper gradient change), corresponding to the lead switch on- and off-states. For $B = 2$ T, the heat flow was $-41.6 \pm 1.2 \mu\text{W}$ in the on-state and $-102.8 \pm 2.08 \mu\text{W}$ in the off-state, yielding an off : on ratio of 2.47. This ratio is representative of the difference between total heat

leaks minus cooling due to demagnetisation briefly before and after the superconducting transition. It can be seen, then, that the on-state switch represents $> 60\%$ of the total heat leak, at $\sim 60 \mu\text{W}$, or a total of $\sim 25 \text{ mJ}$. Thus, reducing the time during demagnetisation in the on-state would represent a significant increase in performance. The main options to achieve this include; using a separate magnet for operating the switch, reducing the field at the switch, or using a switch with higher H_c . The former option is prohibitively complex and costly for the purposes of this project, the second can be achieved by increasing the displacement of the switch from the field centre, or by using a switch with larger dB/dZ , for example a Helmholtz coil, and finally the third option was the primary motivation for testing a niobium switch.

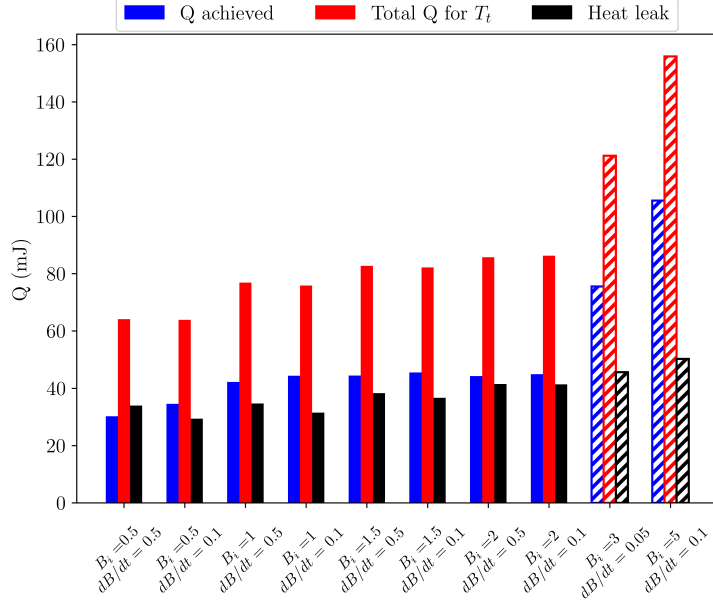


Figure 31: The energy removed by demagnetisation for each run (blue), the energy required to reach the theoretical minimum temperature (red), and the difference between the two/ the heat leak (black). Solid bars represent lead switch runs, hatched represent niobium.

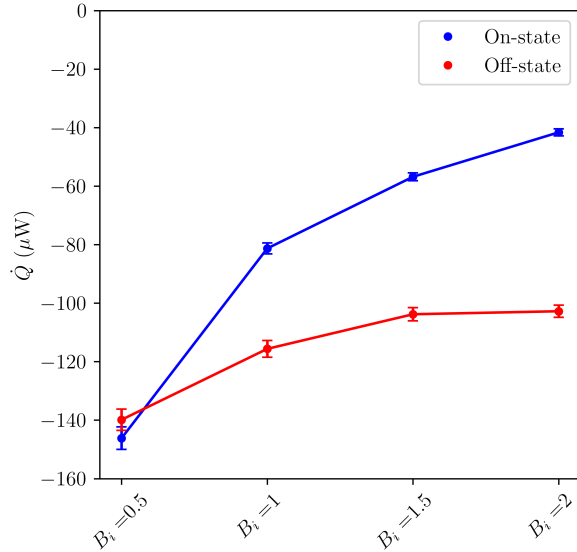


Figure 32: Total heat flow during demagnetisation for $dB/dt = 0.1 \text{ T/min}$ using lead heat switch. Off-state powers shown in red, on state in blue. Off : on ratios are 0.97, 1.42, 1.83 and 2.47 for $B_i = 0.5, 1, 1.5$ and 2 T respectively.

4.4.3 Niobium switch performance

The minimum temperatures achieved using a niobium heat switch are comparable to those using a lead heat switch, despite T_i being larger. The total energy of demagnetisation was 75 and 106 mJ for the 3 T and 5 T demagnetisations, respectively - approximately double that of the lead switch demagnetisations (43 mJ for $B_i = 2$ T, $dB/dt = 0.1$ T/min). The total heat leaks were 45.6 mJ and 50.3 mJ. This improved cooling ability is enabled by the significantly lower off-state thermal conductivity of the niobium switch, as evidenced by the ~half cooling rate from 80 to 4 K (see fig. 33).

An interesting feature in fig. 27 is the ‘bump’ in temperature at $0.6K < T < 0.8K$, both in the presence and absence of applied field. An explanation for this is the enhanced phonon thermal conductivity at low temperatures. These bumps contribute a heat of ~ 1 and 0.5 mJ for the 3 and 5 T demagnetisations, respectively, equating to \sim a few 10s of mK at 450 mK.

The main cause for the improvement in cooling power can be attributed to the increased applied field to destroy the superconducting state, in comparison to lead. Unlike lead, however, there is no clear change in dT/dt signifying a superconducting transition, meaning an on- or off-state heat leak is difficult to quantify. This can be attributed to a more gradual transition from the normal to superconducting state, as is expected of a type II superconductor. This, too, is influenced by the RRR, with higher RRR samples exhibiting a sharper drop in thermal conductivity below H_{c2} [48] [47]. Thus, by using a purer sample than the 99.8% sample used here, a further performance increase would be gained. This, however, opposes the increased H_{c1} and H_{c2} of lower RRR samples. Further experimentation must be carried out with various niobium samples to optimise the purity for use in a one-magnet ADR.

Upon inspection of the niobium ADR setup following the demagnetisations, it was observed that the copper wire linking the pill to the ES had broken. It is unclear when exactly this occurred, however there is a significant gradient shift in the cooling for the niobium heat switch probe (see fig. 33). This was initially thought to correspond to the H_{c2} transition as it corresponds to ~ 10 K at the switch, but could also be attributed to the copper link breaking due to thermal expansion. The copper broke at the point where the crimped part joined the un-crimped wire. To reduce the chance of this failure occurring again, the copper should not be crimped, despite the sacrifice in contact conductivity. The impact of this failure can be qualitatively assessed by comparing the results with those predicted by the improved thermal model (section 4.5.4).

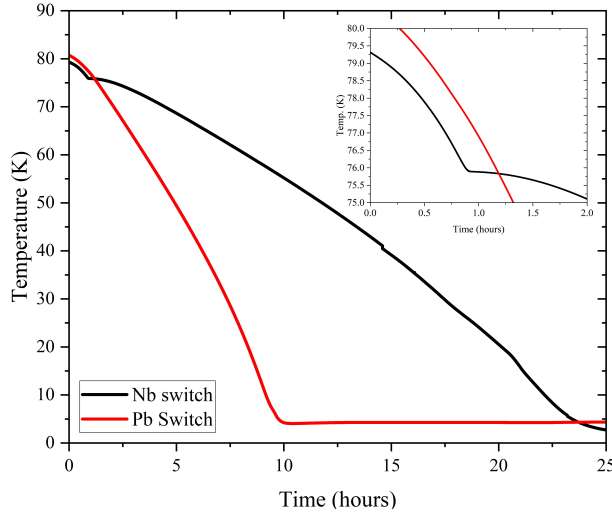


Figure 33: Helium cooling of ADR probes as measured at the ES of the lead heat switch (red) and niobium switch (black). Note the gradient shift for niobium at ~ 76 K (see inset). The gradient shift for the niobium switch at ~ 45 K is due to a brief pause in data recording.

4.5 Modelling

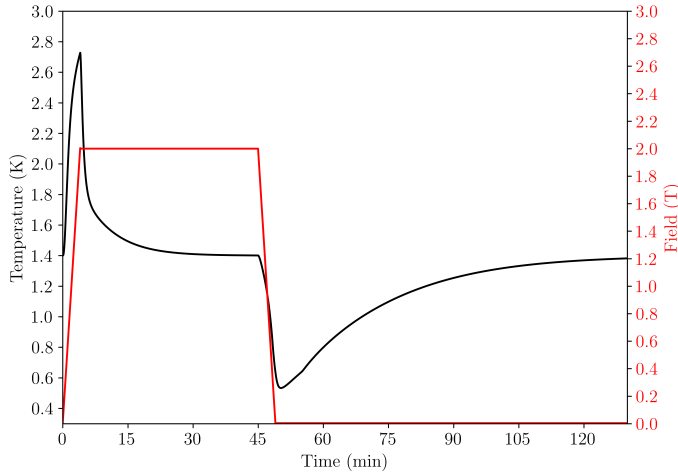
To further understand the heat leaks present in the system, and why the results differed so greatly from the design model, an improved model was made. The goal is to observe the effects of varying different parameters on T_f , and determine the relative magnitudes of the various heat leaks.

4.5.1 Construction of the model

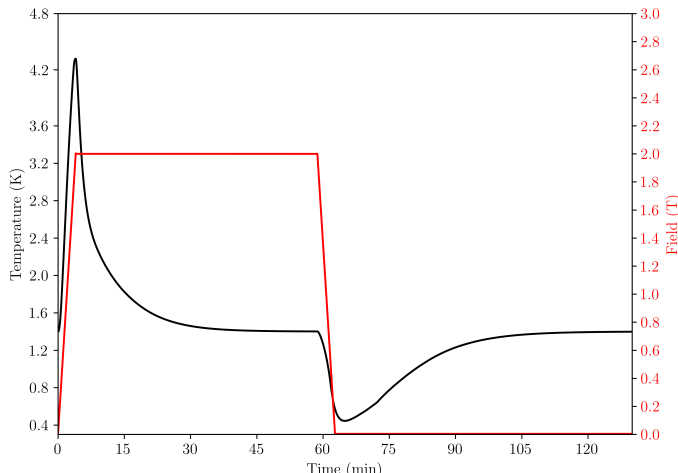
This iteration of the model simulates the full cycle using a simple forward Euler approach, with four main steps: magnetisation, hold for equilibrium to be achieved, demagnetisation, and hold once more. The purpose of this is to introduce the effect of heat leaks due to heat being retained in poorly thermally connected or high heat capacity components, which had not equilibrated with the 1 K pot. To this effect, the heat capacity of the G10 rods is added, along with the temperature as measured at the ES.

Parameter	Value
T_i	1.4 K
B_i	2 T
dB/dt (demag)	-0.5 T/min
dB/dt (mag)	0.5 T/min
n_{frac}	0.1
n_{links}	5
Switch	Lead
Salt	FAA

Table 8: The default parameters used for all modelling, unless stated otherwise.



(a) Model full cycle for a lead heat switch as measured at the ES.
The minimum temperature is 53 mK



(b) Model full cycle for a niobium heat switch as measured at the ES. The minimum temperature is 44 mK.

Figure 34: Example of modelled results using default parameters for a lead and niobium heat switch, FAA pill.

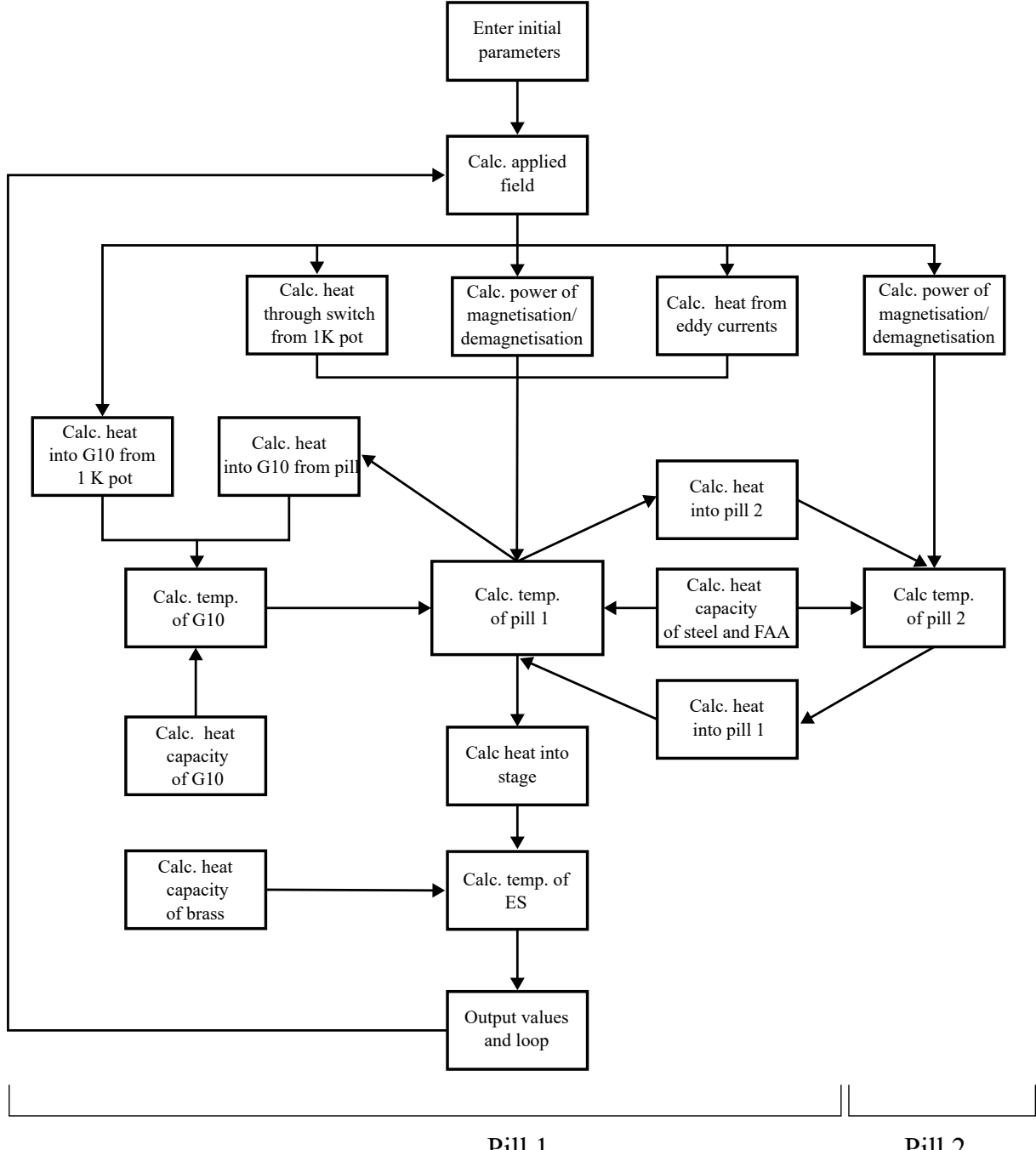
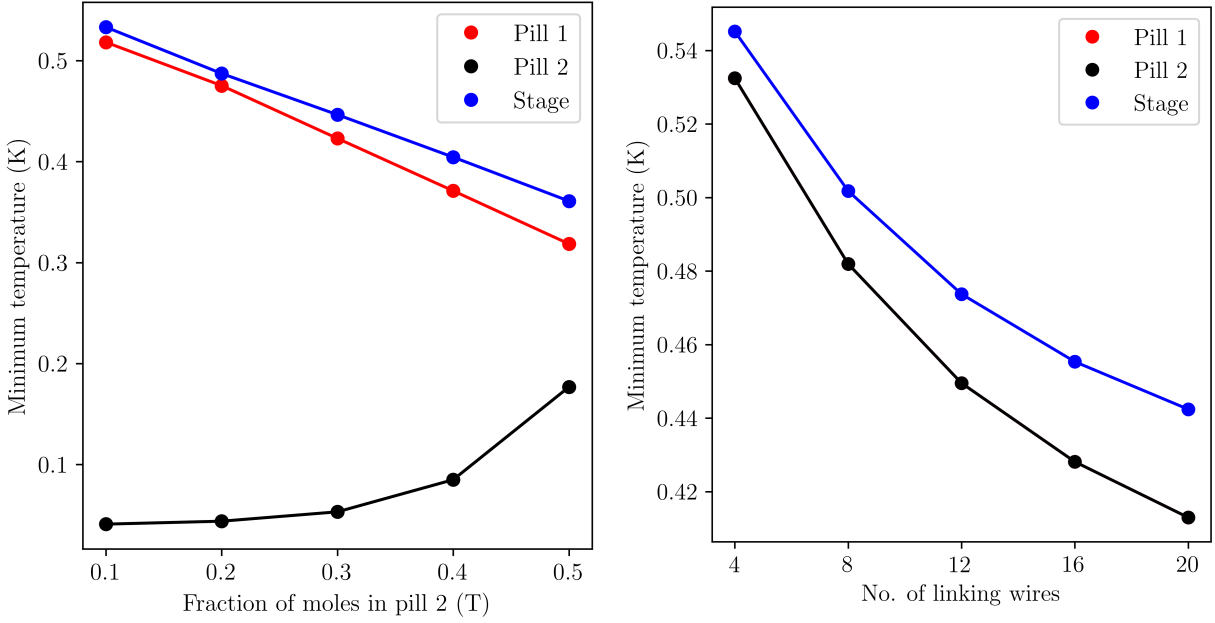


Figure 35: Schematic of ADR model. Calculation of field and temperature-dependent thermal conductivities omitted.

4.5.2 Pill Characterisation

A complication to the construction of the model was the fact that the pill was not constructed as part of this project, but was inherited from a previous group, so no information besides the total number of moles of FAA and thermal bus material is known. To account for this in the model, a second pill was added which is weakly thermally connected to pill 1 fig. 35. The fraction of the total moles of FAA in pill 2, n_{frac} and the thermal contact can then be varied, to qualitatively observe the effect an inhomogeneous pill structure would have. From fig. 36, it can be seen that the presence of a poorly thermally region decreases the minimum temperature achieved, owing to the reduced impact of heat leaks.

Another unknown factor of the pill, is the extent to which the FAA has degraded. When stored at room temperature for long durations of time, FAA can dehydrate, reducing the magnetic moment separation, and thus performance [52]. It is difficult to say with certainty whether this occurred, but the observed maximum temperature from magnetisation only differed from that of the model by $\sim 10\%$.



(a) The effect of varying the fraction of the salt in the pill that is poorly thermally connected to the rest of the pill and the thermal bus. The total number of moles is 0.04. Here, there are 5 linking wires.

(b) The effect of varying numbers of silver wires creating thermal contact between pill 1 and pill 2 ($n_{\text{frac}} = 0.1$). One Ag wire has a conductance of $\sim 1 \times 10^{-5} \text{ W/m/K}$ at 1 K.

Figure 36: The effect of a second pill as part of an inhomogeneous pill structure with a lead heat switch.

4.5.3 Field-dependence

An interesting trend observed experimentally was that a slower rate of demagnetisation consistently yielded lower T_f - opposite to what was expected (see fig. 22c), and even observed in the improved model fig. 37b.

One possible explanation for this is the heat capacity of the structures between the salt and the RO thermometer on the ES. With more gradual cooling, the probe is held at low temperature for a longer time, allowing the components to equilibrate at moderate temperatures for longer (i.e. $\sim 1 \text{ K}$), where the heat leak from the 1 K pot is also not a maximum (following eq. (16)). In the case of a fast demagnetisation, there is insufficient time for all components to equilibrate, causing them to leak heat – even during, or after, cooling. For this to manifest in the model, a finite-element approach would be required, which is beyond the scope of what can be achieved in this project.

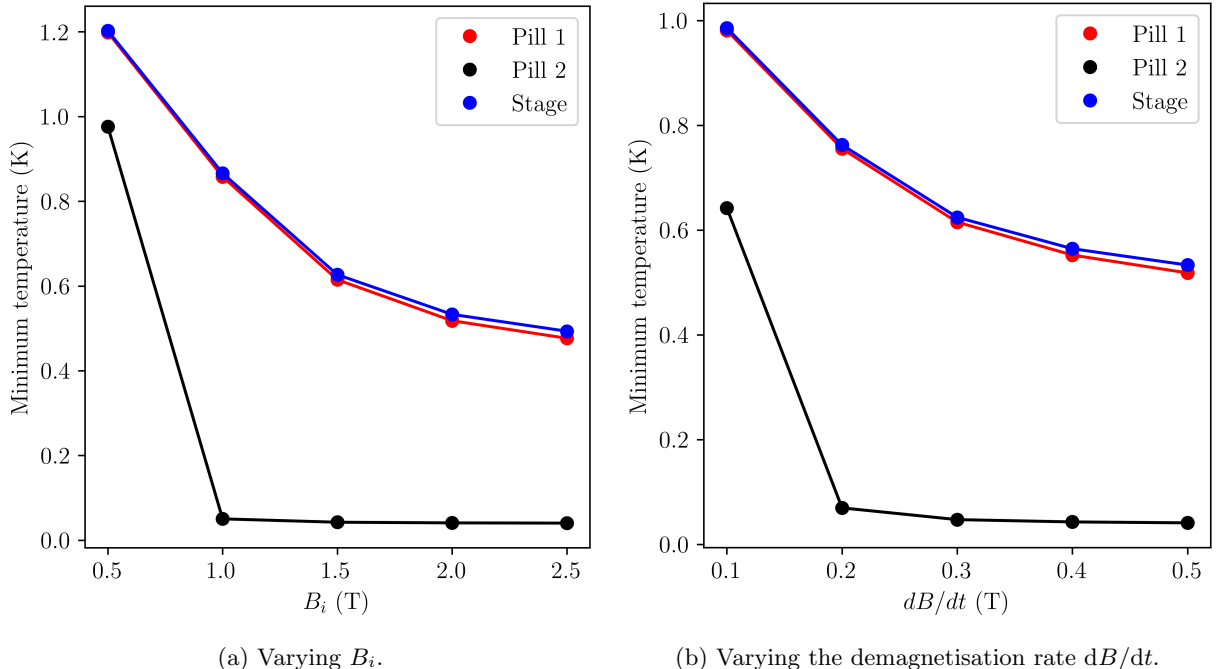


Figure 37: The effect of varying field parameters on the minimum temperature achieved.

4.5.4 Heat leak contributions

From fig. 31, the total heat leaks for each of the magnetisations are given (also see appendix). For the $B_i = 2$ T, $dB/dt = 0.5$ demagnetisation using a lead heat switch, the total heat leak was 41 mJ. By applying the model with the associated parameters, it is estimated that this 41 mJ heat leak consists of components from the switch, through the G10 and from eddy currents of 30.7 mJ, 5.2 mJ and 0.2 mJ respectively (see fig. 44), totalling 36.2 mJ. The total discrepancy is thus 4.8 mJ, with the on-state lead heat leak being ~ 5 mJ higher than the 24.6 mJ calculated in section 4.4.2, implying the off-state contributed ~ 5 mJ in the experiment.

The overall discrepancy can be attributed to the internal heat leaks of the system, such as gradual release of heat from the heat capacities of various components, as well as reduced cooling to contact resistance, and other miscellaneous contributions. It can be seen, then, that the dominant heat leak is the lead heat switch by an order of magnitude.

For the $B_i = 5$ T, $dB/dt = 0.1$ demagnetisation using a niobium heat switch, the total heat leak was 50.3 mJ. Applying the model here results in heat switch, G10 and eddy current contributions of 25.5 mJ, 31 mJ and 0.1 mJ respectively (see fig. 44, right), totalling 56.6 mJ. This is an overestimate by 6.3 mJ, and can primarily be attributed to lack of information on the niobium heat switch. As previously stated, the critical field of niobium is RRR dependent, where lower RRR samples tend to have higher critical fields. The data for the thermal conductivity of niobium for the model was collected using RRR = 196 niobium, most likely \sim double the RRR of the sample we used. In this case, however, due to the long demagnetisation time, the G10 leak was the dominant factor. Comparing the modelled and experimental data, it is unlikely that the change in gradient at ES temperature of 75 K, was, in fact, the copper ES link snapping (see fig. 33). As this shift corresponds to a switch temperature of ~ 11 K, it could represent the superconducting transition of the switch, explaining the long cooling time.

It is important to note that for all modelling, the data for physical parameters is sourced from literature, and thus not wholly accurate to the specific samples used here. A more comprehensive determination of heat leaks would necessitate tests on all the materials used to determine physical quantities such as RRR and thermal conductivity. Furthermore, boundary resistance were not taken into account. A next iteration of the model should account for the most consequential boundary resistances, such as the thermal bus-salt interface.

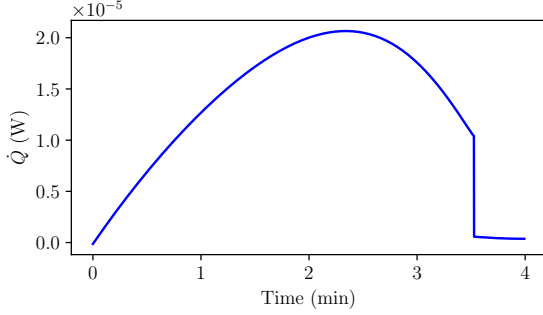


Figure 38: Heat leak through the lead heat switch during demagnetisation, as calculated by the model.

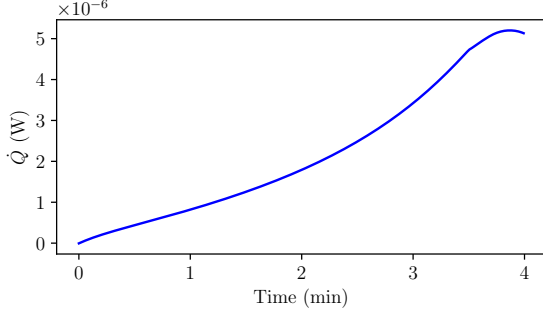


Figure 39: Heat leak from the 1 K pot through the G10 as calculated by the model during demagnetisation with a lead heat switch, default parameters.

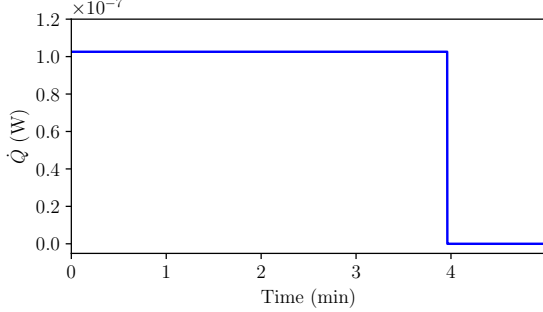


Figure 40: Eddy current heat leak as calculated by the model during demagnetisation with a lead heat switch, default parameters.

Figure 44: Dominant heat leaks during demagnetisation with: a lead heat switch, with $B_i = 2 \text{ T}$, $dB/dt = 0.5 \text{ T/min}$, (left, blue), and a niobium heat switch with $B_i = 5 \text{ T}$, $dB/dt = 0.1 \text{ T/min}$ (right, red). Default values are used for all other parameters (see section 4.5.1).

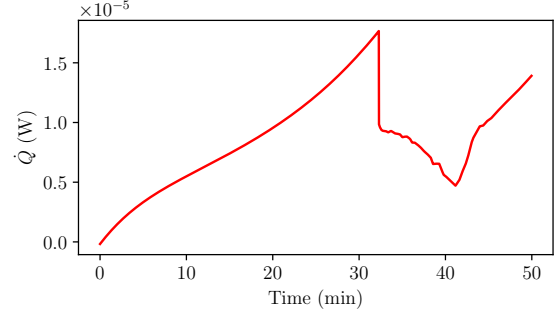


Figure 41: Heat leak through the niobium heat switch during demagnetisation as calculated by the model.

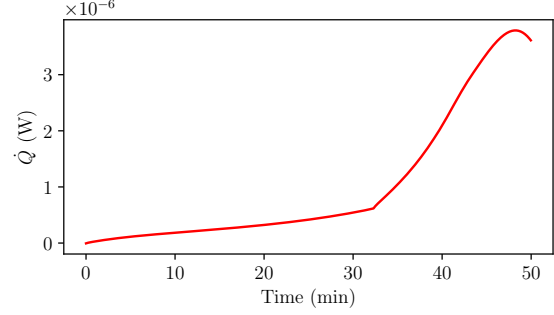


Figure 42: Heat leak from the 1 K pot through the G10 as calculated by the model during demagnetisation with a niobium heat switch.

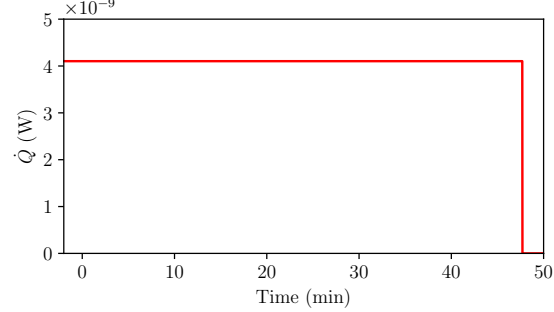


Figure 43: Eddy current heat leak as calculated by the model during demagnetisation with a niobium heat switch.

4.6 Improvements

It has been established that for the demagnetisations using a lead heat switch, conduction through the lead represented the dominant heat leak, and was less efficient in both E_T and E_Q , than the niobium demagnetisations. Thus, the first improvement for a higher performance ADR would be to use an optimised niobium heat switch. The RRR of the sample used in this project is unknown. A useful study would be to test various niobium samples with different RRRs, and observe the experimental result of the competing RRR-dependent effects. One of the few implementations of niobium as a heat switch used a 99.9% pure sample, and was able to achieve an on : off ratio of 650% at 2.5 K [53].

Implementation of the GGHS would circumvent the issue of field-dependent heat leaks entirely, and

with some iteration, could represent a significant improvement.

The second most significant heat leak was the G10 support. As a simple improvement, a piece with a smaller cross-section could be used, as $K \propto r^2$, halving the diameter would result reduce the heat leak by 4 mJ for the $B_i = 2$ T lead demagnetisation and 23 mJ for the $B_i = 5$ T niobium demagnetisation. As the leak is steady-state, the gain is particularly effective for slower demagnetisations or higher B_i . For the lead heat switch demagnetisations, the runs using $dB/dt = 0.1$ T/min consistently achieved a lower minimum temperature, compounding the benefit gained by reducing steady-state heat leaks.

A more significant redesign to the supporting structure would be to suspend the SPH and ES with KevlarTM wires under tension. Although this setup is more complicated than a simple piece of G10, KevlarTM is inexpensive, and the use of it for ADR is well-established [54].

Finally, as this project is centred around ‘single shot’ operation, aiming to achieve the lowest possible temperature, having a large heat capacity is unnecessary. This can be achieved by reducing the size of the salt pill, which has the secondary benefits of lowering thermal bus conductance, and providing more space in the vacuum can to distance the switch further from the pill. Simply by halving the length of the SPH, and the number of moles of FAA, the modelled minimum temperature using the default parameters becomes 0.28 K.

4.7 Conclusions

A functional ADR was constructed at low cost, using readily available materials and simple techniques. A superconducting heat switch was implemented, achieving a minimum temperature of $T_f = 0.43 \pm 0.03$ K for $B_i = 2$ T and $dB/dt = 0.1$ T/min, correlating to a cooling of 43 mJ. The properties of the switch were determined, with H_{c1} being measured as ~ 72 mT, resulting in on-state heat leak of $\sim 60 \mu W$, and an off : on total leak ratio of 2.47. A superconducting niobium heat switch was also implemented, achieving a similar minimum temperature of 0.49 ± 0.03 K from both $T_i = 1.742 \pm 0.005$ and 2.040 ± 0.007 K, corresponding to double the cooling that lead achieved, at 75 and 106 mJ, respectively. Thus, niobium was significantly more effective for off-state operation. A drawback of this implementation of niobium, however, is that an on-state could not be observably established. It is possible that this could be rectified with a higher RRR sample, but more research is needed.

A detailed model was also constructed, which reliably replicated the results observed in the experiment, and provided insight into the various heat leaks in the ADR. Using this, for the lead setup, the main heat leak was found to be through the on-state of the switch, matching the observed results, followed by the heat leak through the G10 support. In the case of the niobium setup, the G10 actually contributed the dominant heat leak. Fortunately, this is an easy design point to iterate upon, with options including using a thinner rod, or KevlarTM wires.

5 Appendix

A Errors

A.1 Magnetoresistance of ROX chip resistors

The ROX chip resistors exhibited a small magnetoresistive effect, which was only noticeable when directly the largest and smallest fields, at $\sim 1\%$ difference between $B = 0.5$ and $B = 2$ T. As such, it was not a significant contribution to the total errors.

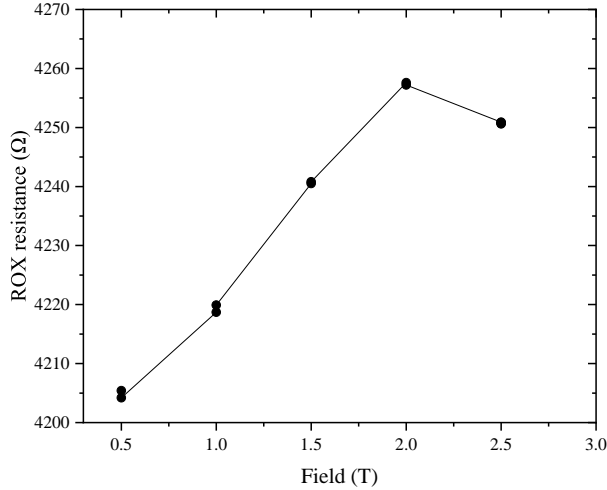


Figure 45: The magnetoresistance of the ROX resistor used for all experiments. $\sim 1\%$ difference between $B = 0.5$ and $B = 2$ T.

A.2 GGHs thermometer error

With increased heat input at the getter, the standard deviation error increased by a factor of ~ 100 . This is due to the competing cooling and heating effects, resulting in an unstable temperature. This was factored into error propagation by summing the variances in the usual way.

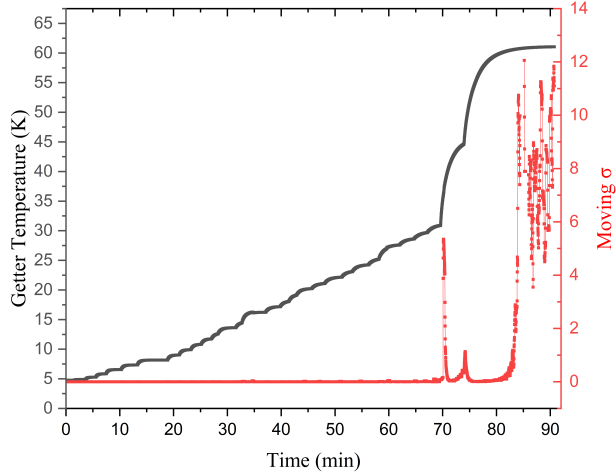


Figure 46: Caption

A.3 Systematic error on ROX

A cubic extrapolation was applied with Python SciPy's optimise 'interp1d' function. This resulted in a peak of systematic error at 1-1.5 K, which gradually then decreased.

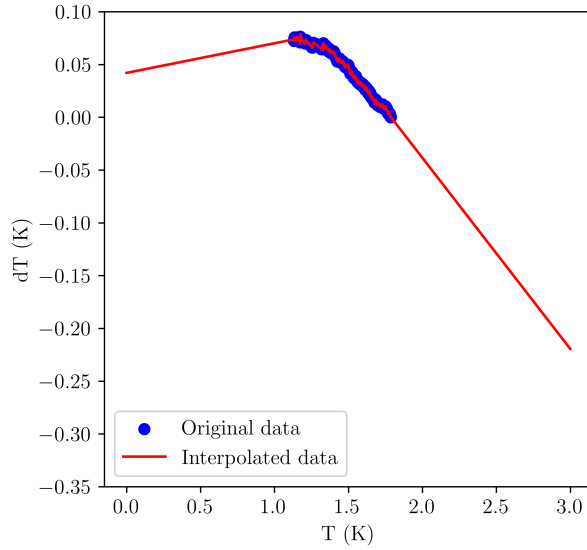


Figure 47: Extrapolated $T_{CX} - T_{RO}$ to find systematic error. Blue is the record data, red is the extrapolation.

B Internal field approximation

The internal field approximation, eq. (11), is only an order-of-magnitude reference point for calculation. Below, the calculated values are compared with experimentally observed values.

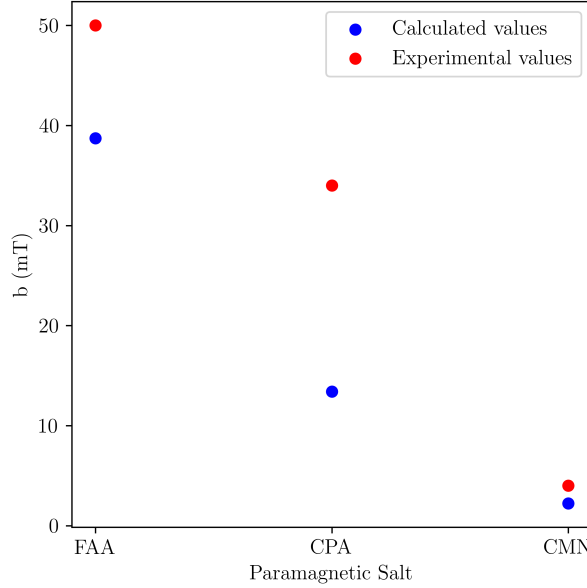


Figure 48: Experimental values compared with those predicted by the free ion approximation (eq. (11)) for various paramagnetic salts.

C Full demagnetisation results

Below are the tabulated results for all lead heat switch demagnetisations.

B_i (T)	dB/dt (T/min)	T_i (K)	T_f (K)	Demagnetisation energy (mJ)
0.5	0.5	1.40 ± 0.03	0.83 ± 0.04	30.1
0.5	0.1	1.40 ± 0.03	0.73 ± 0.04	34.5
1	0.5	1.40 ± 0.03	0.54 ± 0.03	42.1
1	0.1	1.40 ± 0.03	0.45 ± 0.02	44.4
1.5	0.5	1.40 ± 0.03	0.46 ± 0.02	44.3
1.5	0.1	1.40 ± 0.03	0.42 ± 0.02	45.5
2	0.5	1.40 ± 0.03	0.44 ± 0.02	44.2
2	0.1	1.40 ± 0.03	0.43 ± 0.03	44.9
2.5	0.65	1.50 ± 0.02	0.45 ± 0.02	45.6
2.5	0.58	1.50 ± 0.02	0.45 ± 0.02	45.6
2.5	0.05	1.50 ± 0.02	0.42 ± 0.03	46.1

Table 9: Results for all demagnetisations with a lead heat switch. The last three were not discussed above, due to their differing dB/dt s.

D Full model niobium and lead heat leaks

Figure 44 only shows the modelled power data during demagnetisation. The full results over the magnetisation/hold/demagnetisation/hold cycle are below for a lead heat switch and niobium heat switch, respectively. The parameters correspond to those used for fig. 44.

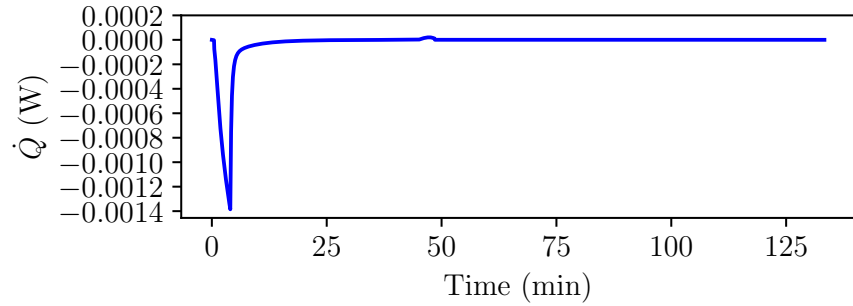


Figure 49: Heat leak through the lead heat switch over the full course of the cycle, as calculated by the model.

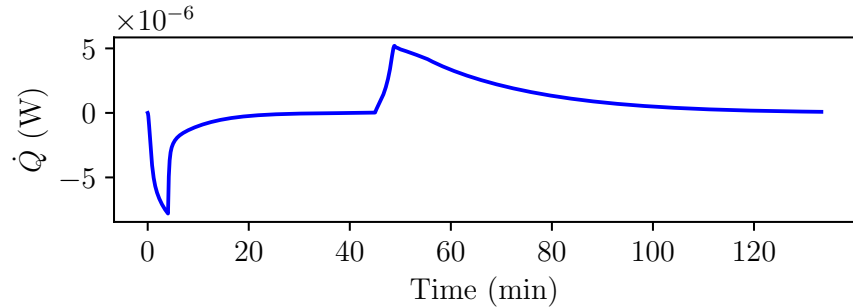


Figure 50: Heat leak from the 1K pot through the G10 as calculated by the model over the full course of the cycle with a lead heat switch, default parameters.

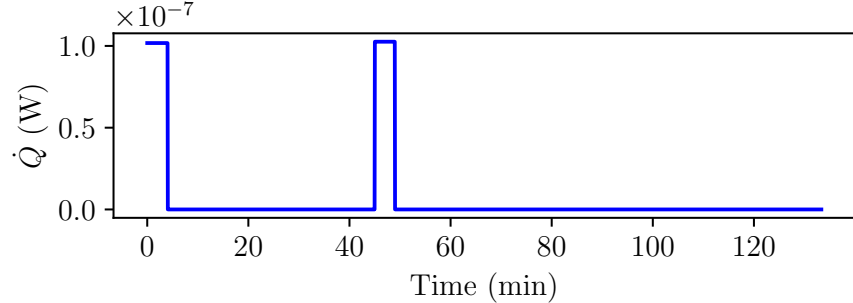


Figure 51: Eddy current heat leak as calculated by the model over the full course of the cycle with a lead heat switch, default parameters.

Figure 52: Full cycle heat leak contributions for a lead heat switch with $B_i = 2\text{T}$, $\text{d}B/\text{dt} = 0.5 \text{ T/min}$.

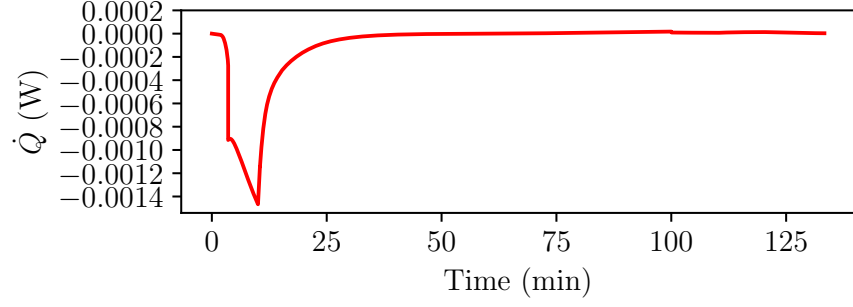


Figure 53: Heat leak through the niobium heat switch over the full course of the cycle, as calculated by the model.

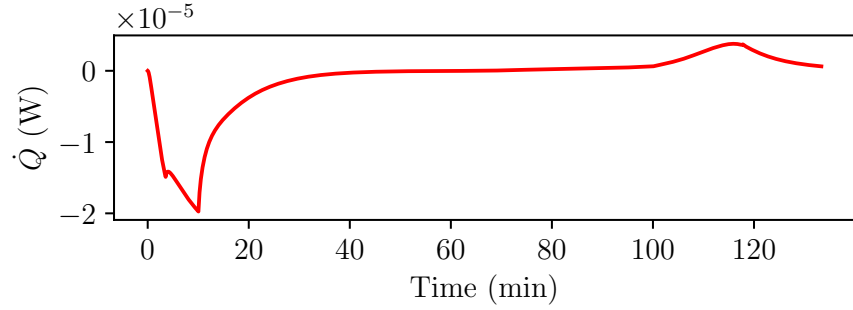


Figure 54: Heat leak from the 1K pot through the G10 as calculated by the model over the full course of the cycle, with a niobium heat switch, default parameters.

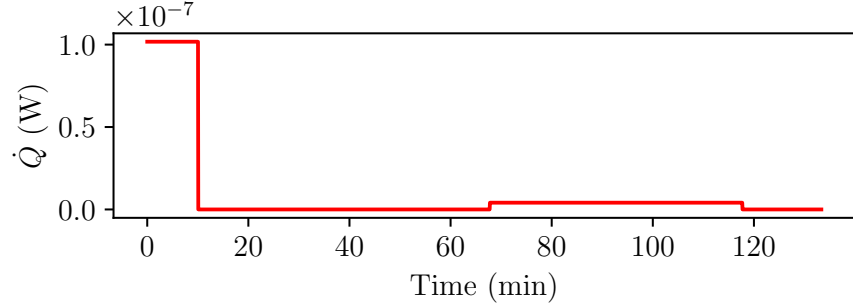


Figure 55: Eddy current heat leak as calculated by the model over the full course of the cycle, with a niobium heat switch, default parameters.

Figure 56: Full cycle heat leak contributions for a niobium heat switch with $B_i = 5\text{T}$, $dB/dt = 0.1 \text{T/min}$.

References

- [1] H-K. Onnes. Investigations into the properties of substances at low temperatures, which have led, amongst other things, to the preparation of liquid helium. *Nobel lecture*, 4:306–336, 1913.
- [2] A. Smith. Who discovered the magnetocaloric effect? warburg, weiss, and the connection between magnetism and heat. *The European Physical Journal H*, 38(4):507–517, 2013.
- [3] A.T. Jones, C.P. Scheller, J.R. Prance, Y.B. Kalyoncu, D.M. Zumbühl, and R.P. Haley. Progress in cooling nanoelectronic devices to ultra-low temperatures. *Journal of low temperature physics*, 201:772–802, 2020.
- [4] J. C. Wheatley. Experimental properties of pure ^3He and dilute solutions of ^3He in superfluid ^4He at very low temperatures. application to dilution refrigeration. In *Progress in low temperature physics*, volume 6, pages 77–161. Elsevier, 1970.
- [5] F. Pobell. *Matter and methods at low temperatures*. Springer Science & Business Media, 2007.
- [6] A.J. Hurd and R.T. Kouzes. Why new neutron detector materials must replace helium-3. *The European Physical Journal Plus*, 129:1–3, 2014.
- [7] C. Kittel and P. McEuen. *Introduction to solid state physics*. John Wiley & Sons, 2018.
- [8] M J Hills. *Thermal transport in tungsten and applications to miniaturised adiabatic demagnetisation refrigerators*. PhD thesis, University College London, 2015.
- [9] P. Wikus, E. Canavan, S. Trowbridge Heine, Koichi Matsumoto, and Takenori Numazawa. Magnetocaloric materials and the optimization of cooling power density. *Cryogenics*, 62:150–162, 2014.
- [10] C. Hagmann and P. Richards. Adiabatic demagnetization refrigerators for small laboratory experiments and space astronomy. *Cryogenics*, 35(5):303–309, 1995.
- [11] C. Hagmann, DJ. Benford, and PL. Richards. Paramagnetic salt pill design for magnetic refrigerators used in space applications. *Cryogenics*, 34(3):213–219, 1994.
- [12] D. Marek, A.C. Mota, and J.C. Weber. Magnetic heat conductance between cmn single crystals and liquid ^3He . *Journal of low temperature physics*, 63:401–421, 1986.
- [13] A.H. Eschenfelder and R.T. Weidner. Saturation effects in paramagnetic resonance. *Physical Review*, 92(4):869, 1953.
- [14] G. W. Wilson and P. T. Timbie. Construction techniques for adiabatic demagnetization refrigerators using ferric ammonium alum. *Cryogenics*, 39(4):319–322, 1999.
- [15] P. A. Bromiley. *Development of an adiabatic demagnetisation refrigerator for use in space*. University of London, University College London (United Kingdom), 2000.
- [16] G. W. Wilson and P. T. Timbie. Construction techniques for adiabatic demagnetization refrigerators using ferric ammonium alum. *Cryogenics*, 39(4):319–322, 1999.
- [17] P. J. Shirron. Applications of the magnetocaloric effect in single-stage, multi-stage and continuous adiabatic demagnetization refrigerators. *Cryogenics*, 62:130–139, 2014.
- [18] J. Bartlett, G. Hardy, and I.D. Hepburn. Design and performance of a fast thermal response miniature chromium potassium alum (cpa) salt pill for use in a millikelvin cryocooler. *Cryogenics*, 65:26–37, 2015.
- [19] E. Ambler and Ralph P. Hudson. Magnetic cooling. *Reports on progress in physics*, 18(1):251, 1955.
- [20] J. Bartlett, G. Hardy, ID. Hepburn, C. Brockley-Blatt, P. Coker, E. Crofts, B. Winter, S. Milward, R. Stafford-Allen, M. Brownhill, et al. Improved performance of an engineering model cryogen free double adiabatic demagnetization refrigerator. *Cryogenics*, 50(9):582–590, 2010.
- [21] P. Kittel. Eddy current heating in magnetic refrigerators. In *Advances in Cryogenic Engineering*, pages 1141–1148. Springer, 1990.
- [22] G.V. Chester and A. Thellung. The law of wiedemann and fritz. *Proceedings of the Physical Society*, 77(5):1005, 1961.

- [23] P. J. Shirron and D. McCammon. Salt pill design and fabrication for adiabatic demagnetization refrigerators. *Cryogenics*, 62:163–171, 2014.
- [24] W. F. Giauque and D. P. MacDougall. Attainment of temperatures below 1° absolute by demagnetization of $Gd_2(SO_4)_3 \cdot 8H_2O$. *Phys. Rev.*, 43:768–768, May 1933.
- [25] J. F. O'Hanlon. *A user's guide to vacuum technology*. John Wiley & Sons, 2005.
- [26] I. Catarino and C. Paine. ^3He gas gap heat switch. *Cryogenics*, 51(1):45–48, 2011.
- [27] R.F. Barron and G.F. Nellis. *Cryogenic heat transfer*. CRC press, 2017.
- [28] N.J. Simon, E.S. Drexler, and R.P. Reed. Properties of copper and copper alloys at cryogenic temperatures. final report. Technical report, National Inst. of Standards and Technology (MSEL), Boulder, CO (US), 1992.
- [29] G .K. White. *Experimental techniques in low-temperature physics*. Clarendon Press, Oxford, 1979.
- [30] C.Y. Ho and T.K. Chu. Electrical resistivity and thermal conductivity of nine selected aisi stainless steels. Technical report, Thermophysical and Electronic Properties Information Analysis Center . . . , 1977.
- [31] A.F. Clark, G.E. Childs, and G.H. Wallace. Electrical resistivity of some engineering alloys at low temperatures. *Cryogenics*, 10(4):295–305, 1970.
- [32] F. Pawlek and D. Rogalla. The electrical resistivity of silver, copper, aluminium, and zinc as a function of purity in the range 4–298 k. *Cryogenics*, 6(1):14–20, 1966.
- [33] Xiao-tong Xi, Jue Wang, Liu-biao Chen, Lu-na Guo, Biao Yang, Yuan Zhou, and Jun-jie Wang. Adsorption characteristics of helium on an activated carbon at 4–10 k and its prospective application in 4 k-class regenerative cryocoolers. *New Carbon Materials*, 34(6):524–532, 2019.
- [34] M.M. Dubinin. Fundamentals of the theory of adsorption in micropores of carbon adsorbents: characteristics of their adsorption properties and microporous structures. *Carbon*, 27(3):457–467, 1989.
- [35] I. Catarino, G. Bonfait, and L. Duband. Neon gas-gap heat switch. *Cryogenics*, 48(1-2):17–25, 2008.
- [36] C. Day. The use of active carbons as cryosorbent. *Colloids and Surfaces A: Physicochemical and Engineering Aspects*, 187:187–206, 2001.
- [37] C.J. Hoffman, F.J. Edeskuty, and E.F. Hammel. Adsorption of He^3 and He^4 on activated charcoal. *The Journal of Chemical Physics*, 24(1):124–130, 1956.
- [38] I. Vázquez, M. P. Russell, D. R. Smith, and R. Radebaugh. Helium adsorption on activated carbons at temperatures between 4 and 76 k. *Advances in Cryogenic Engineering*, pages 1013–1021, 1988.
- [39] A. C. Anderson, G.L. Salinger, and J.C. Wheatley. Thermal conductivity of liquid ^3He . *Physical Review Letters*, 6(9):443, 1961.
- [40] N. D. Mermin and D. M. Lee. Superfluid helium 3. *Scientific American*, 235(6):56–71, 1976.
- [41] R. J. Donnelly and C. F. Barenghi. The observed properties of liquid helium at the saturated vapor pressure. *Journal of physical and chemical reference data*, 27(6):1217–1274, 1998.
- [42] J. D. Reppy. Superfluid helium in porous media. *Journal of Low Temperature Physics*, 87:205–245, 1992.
- [43] P.J. Shirron, E.R. Canavan, M.J. DiPirro, M. Jackson, J. Panek, and J.G. Tuttle. Passive gas-gap heat switches for use in adiabatic demagnetization refrigerators. In *AIP Conference Proceedings*, volume 613, pages 1175–1182. American Institute of Physics, 2002.
- [44] J. Bardeen, G. Rickayzen, and L. Tewordt. Theory of the thermal conductivity of superconductors. *Physical Review*, 113(4):982, 1959.
- [45] MJ. DiPirro and et PJ. Shirron. Heat switches for adrs. *Cryogenics*, 62:172–176, 2014.

- [46] H.R. Kerchner, D.K. Christen, and S.T. Sekula. Critical fields h_c and h_{c2} of superconducting niobium. *Physical Review B*, 24(3):1200, 1981.
- [47] K. Saito et al. Critical field limitation of the niobium superconducting rf cavity. In *The 10th Workshop on RF Superconductivity, Tsukuba, Japan*, pages 583–587, 2001.
- [48] B. K. Moore. *Thermal conductivity of superconducting niobium*. PhD thesis, 1971.
- [49] F. Koechlin and B. Bonin. Parametrization of the niobium thermal conductivity in the superconducting state. *Superconductor Science and Technology*, 9(6):453, 1996.
- [50] O. E. Vilches and J. C. Wheatley. Measurements of the specific heats of three magnetic salts at low temperatures. *Phys. Rev.*, 148:509–516, Aug 1966.
- [51] C. Hagmann and P.L. Richards. Specific heat of stainless steel below $t = 1$ k. *Cryogenics*, 35(5):345, 1995.
- [52] P.T. Timbie, G.M. Bernstein, and P.L. Richards. Development of an adiabatic demagnetization refrigerator for sirtf. *Cryogenics*, 30(3):271–275, 1990.
- [53] M. Yoshida, M. Riad Kasem, A. Yamashita, K. Uchida, and Y. Mizuguchi. Magneto-thermal-switching properties of superconducting nb. *Applied Physics Express*, 16(3):033002, 2023.
- [54] A.T. Serlemitos, B.A. Warner, S. Castles, S.R. Breon, M. San Sebastian, and T. Hait. Adiabatic demagnetization refrigerator for space use. *Advances in Cryogenic Engineering: Part A & B*, pages 1431–1437, 1990.

Certification of ownership of the copyright

This Project Report is presented as part of, and in accordance with, the requirements for the degree of MSci at the University of Bristol, Faculty of Science.

I hereby assert that I own exclusive copyright in the item named below. I give permission to the University of Bristol Library to add this item to its stock and to make it available for consultation in the library, and for inter-library lending for use in another library. I also give consent for this report to made available electronically to staff and students within the University of Bristol. It may be copied in full or in part for any bona fide library or research work. No quotation and no information derived from it may be published without the author's prior consent.

Author	Alex Higginbottom
Title	Cooling to Zero
Date of submission	20.04.2023

I agree that submission of this report constitutes signing of this declaration.

This project/dissertation is the property of the University of Bristol and may only be used with due regard to the rights of the author. Bibliographical references may be noted, but no part may be copied for use or quotation in any published work without the prior permission of the author. In addition, due acknowledgement for any use must be made.